The final publication is available at

https://doi.org/10.1007/s00466-013-0971-3

Additional Information

What-You-Prescribe-Is-What-You-Get orthotropic hyperelasticity

Marcos Latorre · Francisco Javier Montáns

Abstract We present a model for incompressible finite strain orthotropic hyperelasticity using logarithmic strains. The model does not have a prescribed shape. Instead, the energy function shape and the material data of the model are obtained solving the equilibrium equations of the different experiments. As a result the model almost exactly replicates the given experimental data for all six tests needed to completely define our nonlinear orthotropic material. We derive the constitutive tensor and demonstrate the efficiency of the finite element implementation for complex loading situations.

Keywords Hyperelasticity · Incompressible orthotropic materials · Finite Elements · Living tissues · Rubber-like materials

1 Introduction

In the mechanics of deformation of solids, large strain kinematics introduce many difficulties. The first one is the consideration of the adequate strain and stress measures over which to build the constitutive model that represents the behavior of the solid for the problem at hand [1], [2], [3]. Even though once a strain measure is obtained any other strain measure may be readily obtained from the former one [4], [5], the structure of a constitutive equation based on a specific measure implies some hypothesis over the behavior predicted by the model, not only on the form of the stress-strain curves but also on the form of the coupling between components [3]. The second type of consideration relates to the physical and mathematical correctness of the derived constitutive equations which in the small strains context are almost given for granted. For example, in large strain elasticity, care must be exercised in order to preserve energy during closed cycles [6]. Hence, the use of hyperelastic models in nonlinear elasticity is nowadays rather standard in computational mechanics [1].

Hyperelastic behavior is truly elastic because energy is exactly preserved in conservative systems [6]. The reason is that hyperelasticity assumes the existence of a stored energy function (a model) of the total deformations. The key for energy preservation is at the same time the reason of the main difficulty. Stored energies cannot be measured. Hence, a specific function dependency must be assumed (i.e. a hyperelastic model). From the derivative of such function, stresses are obtained for a given strain tensor. Of course the resulting stress-strain relation may, or may not be close to the actual behavior of the material at hand. Therefore, many different stored energy functions have been proposed for different classes of materials. For isotropic materials the models of Ogden [7], Mooney [8] and Rivlin [9], Blatz and Ko [10], Yeoh [11] and Arruda and Boyce [12] are well known. Ogden's proposal [7] is a very commonly used model because a variable number of parameters may be obtained by an optimization algorithm [13], [3] in order to very closely capture the global behavior of most isotropic nonlinear elastic materials. For transversely isotropic materials or orthotropic materials the situation is not so optimal. Some models have been pro-

Marcos Latorre
Escuela Técnica Superior de Ingenieros Aeronáuticos, Universidad Politécnica de Madrid
Pza.Cardenal Cisneros, 28040-Madrid, Spain
E-mail: m.latorre.ferrus@upm.es

Francisco Javier Montáns
Escuela Técnica Superior de Ingenieros Aeronáuticos, Universidad Politécnica de Madrid
Pza.Cardenal Cisneros, 28040-Madrid, Spain
Tel.: +34 637908304
E-mail: fco.montans@upm.es

posed for transversely isotropic materials [14], [15] and for orthotropic materials [16], [17], [18]. However, the results are not so successful as for the isotropic case.

A significative change in the way the problem is addressed is given in the work of Sussman and Bathe [19]. In their work, instead of directly assuming a stored energy function form (i.e. the shape) they interpolate *experimental* stress-strain data. In order to interpolate such data they use cubic splines. The key to the procedure is to solve the equilibrium equation of the particular experiment from which the stress-strain data is obtained to compute the derivative of the stored energy function at each point. Once this stored energy function is obtained, it is of course valid in any other situation, different from the experimental setup. The main mathematical difficulty is that the equilibrium equation is nonlinear and mostly recursive. However, the use of an inversion formula originally given by Kearsley and Zapas [20] provides a gate to the solution of such equation for the isotropic incompressible case.

The work of Sussman and Bathe [19] was developed for isotropic hyperelastic materials, where the above mentioned material models are often considered satisfactory if an adequate parameter fitting procedure is performed. However, the methodology is more far reaching because it can be extended both to incompressible transversely isotropic materials [21] and to incompressible orthotropic materials under some conditions. For these materials, less satisfactory constitutive models are available, so the contribution for these two classes of materials is important, specially if the experimental stress-strain data is "exactly" predicted by the model. In summary, it is a WY*P*IWYG (What-You-Prescribe-Is-What-You-Get) procedure or model.

The extension of the Sussman-Bathe model to incompressible transversely isotropic materials and incompressible orthotropic materials is by no means evident. The number of experimental curves to prescribe and to be reproduced by this type of models is three for the transversely isotropic model and six for the orthotropic model. Thus, the number of distinct equilibrium equation sets from experiments is three and six respectively. Furthermore, the lack of isotropy invalidates the original inversion formula of Kearsley and Zapas [20], which must be reformulated for a more general case [21]. The procedure also requires some stored energy uncoupling hypothesis in the spirit of (but different from) the Valanis-Landel hypothesis. For such hypothesis, the use of logarithmic strain measures and a proper understanding of their components is evident [22]. In Reference [21] we developed the procedure for transversely isotropic materials, where the excellent capability of the model to predict actual experimental behavior

was apparent. The purpose of the present manuscript is to extend the procedure to the even more complex orthotropic case.

The layout of the manuscript is as follows. First, in order to bring the manuscript as self-contained as possible, we briefly review the piecewise nonuniform spline interpolation (which slightly differs from the one presented in Ref. [21]), the new inversion formula and the uncoupled form of the stored energy function that we propose for the orthotropic case. We also pay special attention to the logarithmic strain and stress measures employed in our orthotropic model. Once the basic ingredients of the formulation have been introduced, we describe the procedure for obtaining the different terms of the stored energy from stress-strain experimental data taken from different typical sets of experiments. Then, through some examples we show the predictive capabilities of the model. Finally, we include an academic example to show the finite element implementation of the model and the efficiency of the algorithm in complex loading situations.

2 Building blocks

In this section we introduce the basic ingredients of the formulation which will be used in the remaining part of the paper. The understanding of these "building blocks" is crucial to understand the overall procedure.

2.1 Spline-based piecewise interpolation used in the model

All the functions of the model presented in this work are built using a spline-based interpolation methodology. The aim of this subsection is to show how to interpolate a set of experimental data points using piecewise cubic splines. The procedure detailed herein is valid for nonuniform subintervals, hence it is more general than the one presented in Ref. [21]. Evidently, for equally spaced points (abscissae), both procedures coincide.

Let $\{x_i, y_i\}$, with $i = 1, ..., N + 1$, be the set of points to be interpolated, where x_i usually corresponds to strain measures and y_i to stress measures. Cubic splines interpolate these points by means of cubic polynomials, which will be enforced to fulfill some smoothness conditions. For each subinterval $[x_i, x_{i+1}]$, a new normalized variable $\xi = (x - x_i) / (x_{i+1} - x_i)$ is used, so each one of the interpolating polynomials, i.e. $P_i(\xi)$ with $i = 1, ..., N$, is defined in the corresponding uniform unit-length subinterval $[\xi_i, \xi_{i+1}] = [0, 1]$. The cu-

bic polynomial defined within the ith subinterval is

$$P_i(\xi) = a_i + b_i\xi_i + c_i\xi_i^2 + d_i\xi_i^3$$
$$0 \le \xi \le 1 \qquad i = 1, ..., N \tag{1}$$

The piecewise function, formed by N splines, has to fulfill several requirements. These requirements, together with two extra end conditions, will let us calculate the $4 \times N$ polynomial coefficients. First of all, simply make

$$a_i = y_i \quad , \qquad i = 1, ..., N$$
$$a_N + b_N + c_N + d_N = y_{N+1} \tag{2}$$

so that the resulting function exactly passes through the measured data points. Aside, continuity of the function at each break point x_i implies that

$$a_{i-1} + b_{i-1} + c_{i-1} + d_{i-1} = a_i \quad , \qquad i = 2, ..., N \tag{3}$$

Continuity of the first and second derivatives of the spline-based function provides

$$\frac{b_{i-1} + 2c_{i-1} + 3d_{i-1}}{h_{i-1}} = \frac{b_i}{h_i} \quad , \qquad i = 2, ..., N \tag{4}$$

$$\frac{2c_{i-1} + 6d_{i-1}}{h_{i-1}^2} = \frac{2c_i}{h_i^2} \quad , \qquad i = 2, ..., N \tag{5}$$

where $h_i = x_{i+1} - x_i$ is the length of the subinterval $[x_i, x_{i+1}]$ and appears in the two previous equations because the smoothness requirements must be imposed to the derivatives of the interpolating function with respect to x. Note that for equally spaced subintervals, h_i is the same for $i = 1, ..., N$ and the equations and the procedure detailed in Ref. [21] are recovered. However, using the present procedure the intervals do not have to be equal in length. At this point, only two more equations are needed to close the system. Several end conditions can be used, such as prescribing the value of the first or second derivatives at both ends or imposing any specific requirement to the first and last polynomial. The usual approach is to simply make the second derivative of the 1st and Nth splines equal to zero at x_1 and x_{N+1}, respectively (which is known as "natural" end condition), or also impose third-derivative continuity between the first and second splines at x_2 and between the second to last and last splines at x_N. For this last case, the first (or last) two splines represent the same cubic polynomial, hence the name "not-a-knot".

To solve these equations, first note that from Eqs. (3) and (4) we can obtain

$$\left. \begin{array}{l} c_{i-1} = 3(y_i - y_{i-1}) - 2Y_{i-1} - \dfrac{h_{i-1}}{h_i}Y_i \\[2mm] d_{i-1} = -2(y_i - y_{i-1}) + Y_{i-1} + \dfrac{h_{i-1}}{h_i}Y_i \end{array} \right\} \quad i = 2, ..., N \tag{6}$$

where Eq. $(2)_1$ has been used and we have denoted $b_i = Y_i$. The substitution of these two last expressions in Eqs. (5) provides the following $N-1$ ($i = 2, ..., N$) equations

$$\frac{h_i^2}{h_{i-1}^2}Y_{i-1} + 2\left(\frac{h_i}{h_{i-1}} + 1\right)Y_i + \frac{h_i}{h_{i+1}}Y_{i+1} =$$
$$= -3\frac{h_i^2}{h_{i-1}^2}y_{i-1} + 3\left(\frac{h_i^2}{h_{i-1}^2} - 1\right)y_i + 3y_{i+1} \tag{7}$$

where the unknowns are the $N+1$ values Y_i. The equations for $i = 1$ and $i = N + 1$ are obtained from the selected type of end conditions. For example, for "natural" end conditions these two equations are

$$2Y_1 + \frac{h_1}{h_2}Y_2 = 3(y_2 - y_1) \tag{8}$$

$$Y_N + 2\frac{h_N}{h_{N+1}}Y_{N+1} = 3(y_{N+1} - y_N) \tag{9}$$

Once the values $Y_1, ..., Y_{N+1}$ are calculated from the previous linear system (or any other for different end conditions), Equations (6) evaluated for $i = 2, ..., N+1$ provide the remaining spline coefficients $c_1, ..., c_N$ and $d_1, ..., d_N$. Finally, we note that the value assigned to h_{N+1}, which appears in the previous equations and which is initially unknown, is arbitrary and that the solution coefficients obtained are independent of the selected value for h_{N+1}. One possible choice is just to take $h_{N+1} = h_N$.

2.2 The inversion formula

In this paper we will have to solve a particular type of equations in which the unknown function cannot directly be factored out. In these cases, an "inversion formula" (see Refs. [19], [21]) is to be used.

The type of these specific equations is as follows. Consider two known functions $f(x)$ and $y(x)$, which relates to another unknown function $g(x)$ through the following equation

$$f(x) = g(x) - g(y(x)) \tag{10}$$

all the functions being continuous in all the domain of interest. Then, obviously

$$f(x) = g(x) - g(y(x)) \tag{11}$$

$$f(y(x)) = g(y(x)) - g\left(y^{(2)}(x)\right) \tag{12}$$

$$\vdots$$

$$f\left(y^{(K)}(x)\right) = g\left(y^{(K)}(x)\right) - g\left(y^{(K+1)}(x)\right) \tag{13}$$

where the notation $y^{(k)}(x)$ has been used to denote the kth recursive composition of function $y(x)$, that is

$$y^{(k)}(x) = \underbrace{y(y(...(y(x))...))}_{k} \qquad k \geq 1 \qquad (14)$$

For $k = 0$, the convention $y^{(0)}(x) = x$ is taken.

The sum of both sides of the set of Eqs. (11)–(13) provides the still implicit relation

$$\sum_{k=0}^{K} f\left(y^{(k)}(x)\right) = g(x) - g\left(y^{(K+1)}(x)\right) \qquad (15)$$

which yields an explicit, useful, solution for $g(x)$ if $\lim_{K \to \infty} g\left(y^{(K)}(x)\right) = 0$, i.e.

$$g(x) = \sum_{k=0}^{\infty} f\left(y^{(k)}(x)\right) \qquad (16)$$

As we will see below, the functions $f(x)$, $y(x)$ and $g(x)$ that we will employ are such that $f(0) = 0$, $|y(x)| < |x|$ and $g(0) = 0$. Therefore, $g\left(y^{(\infty)}(x)\right) = g(0) = 0$ and Eq. (16) can effectively be regarded an exact solution of Eq. (10).

The elegant form Eq. (16) is due to Sussman, who improved our original proposal (Ref. [21]).

2.3 Assumed uncoupled decomposition of the stored energy function

In Ref. [21], motivated by the initial work of Sussman and Bathe for incompressible isotropic hyperelastic materials [19], we present a spline-based strain energy description separable in terms of logarithmic strains to model isochoric transversely isotropic materials. In that work, we take advantage of the assumed additive decomposition of the stored energy function, the spline interpolation methodology and the application of the inversion formula, to reproduce very accurately (exactly in practical cases) the measured stress-strain data points obtained from experiments. Several possibilities of user-prescribed experimental curves are allowed as input data to define the model, which are properly addressed therein.

In this subsection, we extend the uncoupled formulation presented in Ref. [21] to orthotropic symmetry conditions. We will see within next sections that, with the proposed extension, the model is capable of providing a very good fitting for a set of six experimental curves, which will be used to entirely define our orthotropic model.

The orthotropic nature of a material is characterized by the existence of three orthogonal symmetry planes with respect to which the mechanical behavior of the material preserves the symmetries. The unit normal vectors to those planes form a right-handed basis $\boldsymbol{X}_{pr} = \{\boldsymbol{e}_1, \boldsymbol{e}_2, \boldsymbol{e}_3\} = \{\boldsymbol{a}_0, \boldsymbol{b}_0, \boldsymbol{c}_0\}$ defining the preferred orthotropic directions in the reference material configuration. Obviously, this direction dependence has to be included into the energy function for these type of materials in order to be able to reproduce the corresponding symmetries and to fulfill the required invariance principles. Since $\boldsymbol{c}_0 = \boldsymbol{a}_0 \times \boldsymbol{b}_0$, the explicit dependence of the hyperelastic strain energy function reduces to $\mathcal{W}(\boldsymbol{E}, \boldsymbol{a}_0, \boldsymbol{b}_0)$, where in our case $\boldsymbol{E}$ is the material logarithmic (Hencky) strain tensor for the considered isochoric deformation, and $\mathcal{W}(\boldsymbol{E}, \boldsymbol{a}_0, \boldsymbol{b}_0)$ can be regarded a function of seven invariants expressed in terms of the components of $\boldsymbol{E}$ in the preferred orthotropy directions $\boldsymbol{X}_{pr}$ (cf. Ref. [3]), that is

$$\mathcal{W} = \mathcal{W}(E_{11}, E_{22}, E_{33}, E_{12}^2, E_{23}^2, E_{31}^2, E_{12}E_{23}E_{31}) \quad (17)$$

where $E_{ij} = \boldsymbol{e}_i \cdot \boldsymbol{E}\boldsymbol{e}_j$, with $i, j = \{1, 2, 3\}$. Due to the incompressibility constraint $tr(\boldsymbol{E}) = \boldsymbol{E} : \boldsymbol{I} = E_{11} + E_{22} + E_{33} = 0$ and the list of independent invariants reduces to six. The fully uncoupled decomposition of the strain energy function that we propose is separable in terms of six of these seven invariants and it reads

$$\mathcal{W} = \omega_{11}(E_{11}) + \omega_{22}(E_{22}) + \omega_{33}(E_{33}) + \\ + 2\omega_{12}(E_{12}) + 2\omega_{23}(E_{23}) + 2\omega_{31}(E_{31}) \qquad (18)$$

where the terms ω_{ij} for $i \neq j$ are required to be symmetric functions and where the dependence on the shear-strain-coupled-invariant $E_{12}E_{23}E_{31}$ is not included. The six different functions involved in Eq. (18) can be determined from a proper set of six user-prescribed curves obtained from experimental testing, as it is explained below. Regarding this decomposition, note that the number of (initially unknown) independent functions coincide with the number of independent material parameters which define the fully uncoupled isochoric behavior of orthotropic materials within the small strain framework. Also, it can be observed that for finite deformations in which the principal directions of strain are coincident with the preferred material directions, Eq. (18) reduces to

$$\mathcal{W} = \omega_{11}(E_1) + \omega_{22}(E_2) + \omega_{33}(E_3) \qquad (19)$$

which can be considered a generalization of the Valanis-Landel hypothesis (see Refs. [23], [3]) applicable to incompressible orthotropic hyperelastic materials. Advantage of this fact can be taken in order to isolate the components of the strain energy function (we note that the adoption of the form of Eq. (18) means a special (un)coupling of the different terms). However, a further

motivation for the choice of the decomposition given in Eq. (18) (additive, with uncoupled addends in terms of logarithmic strain components and non-dependent on $E_{12}E_{23}E_{31}$) will be apparent in Section 4.1, where we show that it exactly applies in some specific cases. Then in Sections 4.2 and 4.3, we show the very good prediction capability of this model. For the sake of simplicity, symmetry considerations in Eq. (18) have not been explicitly written. We take them into consideration in Section 2.5, where the spectral decomposition of second-order stress tensors and fourth-order elasticity tensors are obtained.

2.4 The stress tensor work-conjugate to the logarithmic strain tensor

Let ^0V and ^tV be the original volume and deformed volume at time t of a body, respectively. A point representing an infinitesimal volume is denoted in the reference configuration by $^0\boldsymbol{x}$, and in the current configuration by

$$^t\boldsymbol{x} = {}^0\boldsymbol{x} + {}^t\boldsymbol{u} \tag{20}$$

where $^t\boldsymbol{u}$ are the displacements at time t. The deformation gradient is defined by

$$^t_0\boldsymbol{X} = \frac{\partial^t\boldsymbol{x}}{\partial^0\boldsymbol{x}} \tag{21}$$

—note that frequently this tensor is denoted by $\boldsymbol{F}$ but we use the notation of Refs. [1] and [2]. Consider also the Right Polar Decomposition of the deformation gradient

$$^t_0\boldsymbol{X} = {}^t_0\boldsymbol{R}\,{}^t_0\boldsymbol{U} \tag{22}$$

where $^t_0\boldsymbol{R}$ is the rotation tensor and $^t_0\boldsymbol{U}$ is the material stretch tensor. Work conjugacy may be very easily motivated by the existence of a stored energy $\mathcal{W}$ per unit reference volume ^0V and by the mechanical power conservation principle (in the equations to follow we omit the time left-indices)

$$\mathcal{P} = \dot{\mathcal{W}} = \boldsymbol{S} : \dot{\boldsymbol{A}} = \boldsymbol{T} : \dot{\boldsymbol{E}} \tag{23}$$

where $\boldsymbol{A} = 1/2(\boldsymbol{X}^T\boldsymbol{X} - \boldsymbol{I})$ is the Green-Lagrange strain tensor, $\boldsymbol{S} = \partial\mathcal{W}/\partial\boldsymbol{A}$ is the Second Piola Kirchhoff stress tensor, $\boldsymbol{E} = \ln\boldsymbol{U}$ is the already mentioned Hencky strain tensor and $\boldsymbol{T} = \partial\mathcal{W}/\partial\boldsymbol{E}$ is the Generalized Kirchhoff stress tensor, which is work-conjugate of $\boldsymbol{E}$ in the most general anisotropic case. Note that the preferred directions $\{\boldsymbol{a}_0, \boldsymbol{b}_0, \boldsymbol{c}_0\}$ are assumed to remain constant in the material configuration and that possible additional terms to be considered in Eq. (23) due to the rotation of the anisotropy axes are not considered herein.

For a detailed understanding of these additional terms in the context of large strain anisotropic elastoplasticity, the reader is referred to Refs. [4] and [24].

There exist a mapping between the stress tensors $\boldsymbol{S}$ and $\boldsymbol{T}$. This mapping can be easily obtained from the comparison of tensors $\dot{\boldsymbol{A}}$ and $\dot{\boldsymbol{E}}$ expressed in spectral form, which yields (cf. Ref. [5])

$$\dot{\boldsymbol{A}} = \frac{\partial\boldsymbol{A}}{\partial\boldsymbol{E}} : \dot{\boldsymbol{E}} = \mathbb{M}\frac{\dot{\boldsymbol{A}}}{\dot{\boldsymbol{E}}} : \dot{\boldsymbol{E}} \tag{24}$$

$$\frac{\partial\boldsymbol{A}}{\partial\boldsymbol{E}} = \mathbb{M}\frac{\dot{\boldsymbol{A}}}{\dot{\boldsymbol{E}}} = \sum_{i=1}^{3}\lambda_i^2\,\boldsymbol{M}_i \otimes \boldsymbol{M}_i +$$
$$+\sum_{i=1}^{3}\sum_{j\neq i}\frac{\lambda_j^2 - \lambda_i^2}{2\left(\ln\lambda_j - \ln\lambda_i\right)}\,\boldsymbol{M}_{ij}^S \otimes \boldsymbol{M}_{ij}^S \tag{25}$$

where λ_i are the principal stretches and

$$\boldsymbol{M}_{ij}^S = \frac{1}{2}\left(\boldsymbol{N}_i \otimes \boldsymbol{N}_j + \boldsymbol{N}_j \otimes \boldsymbol{N}_i\right) = \boldsymbol{M}_{ji}^S \tag{26}$$

$$\boldsymbol{M}_i = \boldsymbol{M}_{ii}^S = \boldsymbol{N}_i \otimes \boldsymbol{N}_i \tag{27}$$

are expressed in terms of the principal directions of deformation in the material description $\boldsymbol{N}_i$. Note that the tensor $\mathbb{M}\frac{\dot{\boldsymbol{A}}}{\dot{\boldsymbol{E}}}$ has minor and major symmetries and can, therefore, be stored in the common compact form used for constitutive tensors. For the special case of $\lambda_i = \lambda_j$ for $i \neq j$, the following result is to be used

$$\lim_{\lambda_j\to\lambda_i}\frac{\lambda_j^2 - \lambda_i^2}{2\left(\ln\lambda_j - \ln\lambda_i\right)} = \lambda_i^2 \tag{28}$$

Hence, using Eqs. (23) and (24) we obtain

$$\boldsymbol{S} : \left(\mathbb{M}\frac{\dot{\boldsymbol{A}}}{\dot{\boldsymbol{E}}} : \dot{\boldsymbol{E}}\right) = \left(\boldsymbol{S} : \mathbb{M}\frac{\dot{\boldsymbol{A}}}{\dot{\boldsymbol{E}}}\right) : \dot{\boldsymbol{E}} = \boldsymbol{T} : \dot{\boldsymbol{E}} \quad\Rightarrow$$
$$\Rightarrow \quad \boldsymbol{T} = \boldsymbol{S} : \mathbb{M}\frac{\dot{\boldsymbol{A}}}{\dot{\boldsymbol{E}}} = \mathbb{M}\frac{\dot{\boldsymbol{A}}}{\dot{\boldsymbol{E}}} : \boldsymbol{S} \tag{29}$$

A relationship between the Generalized Kirchhoff stress tensor $\boldsymbol{T}$ and the rotated Kirchhoff stress tensor $\bar{\boldsymbol{\tau}} = \boldsymbol{R}^T\boldsymbol{\tau}\boldsymbol{R}$ ($\boldsymbol{\tau} = J\boldsymbol{\sigma}$ being the Kirchhoff stress tensor, $J = \det\boldsymbol{X}$ the jacobian determinant of the deformation and $\boldsymbol{\sigma}$ the Cauchy stress tensor) is obtained if we rewrite the stress power, Equation (23), as

$$\mathcal{P} = \dot{\mathcal{W}} = \boldsymbol{T} : \dot{\boldsymbol{E}} = \bar{\boldsymbol{\tau}} : \bar{\boldsymbol{d}} \tag{30}$$

where $\bar{\boldsymbol{d}} = \boldsymbol{R}^T\boldsymbol{d}\boldsymbol{R}$ is the rotated deformation rate tensor, which is power-conjugate of $\bar{\boldsymbol{\tau}}$. Since $\boldsymbol{d} = \boldsymbol{X}^{-T}\dot{\boldsymbol{A}}\boldsymbol{X}^{-1}$ then

$$\bar{\boldsymbol{d}} = \mathbb{M}\frac{\bar{\boldsymbol{d}}}{\dot{\boldsymbol{A}}} : \dot{\boldsymbol{A}} \tag{31}$$

where the full symmetric fourth-order mapping tensor $\mathbb{M}^{\bar{\boldsymbol{d}}}_{\dot{\boldsymbol{A}}}$ is

$$\left(\mathbb{M}^{\bar{\boldsymbol{d}}}_{\dot{\boldsymbol{A}}}\right)_{ijkl} = \frac{1}{2}\left(U^{-1}_{ik}\,U^{-1}_{jl} + U^{-1}_{il}\,U^{-1}_{jk}\right) \tag{32}$$

The spectral decomposition of the tensor $\mathbb{M}^{\bar{\boldsymbol{d}}}_{\dot{\boldsymbol{A}}}$ may be readily obtained from Eq. (32) using the components of $\boldsymbol{U}^{-1}$ in the Lagrangian basis, giving as a result

$$\mathbb{M}^{\bar{\boldsymbol{d}}}_{\dot{\boldsymbol{A}}} = \sum_{i=1}^{3}\sum_{j=1}^{3}\lambda_i^{-1}\lambda_j^{-1}\;\boldsymbol{M}^S_{ij}\otimes\boldsymbol{M}^S_{ij} \tag{33}$$

By simply substitution of Eqs. (31), first, and (24), then, in Eq. (30) we obtain

$$\bar{\boldsymbol{\tau}}:\bar{\boldsymbol{d}} = \bar{\boldsymbol{\tau}}:\left(\mathbb{M}^{\bar{\boldsymbol{d}}}_{\dot{\boldsymbol{A}}}:\dot{\boldsymbol{A}}\right) = \left(\bar{\boldsymbol{\tau}}:\mathbb{M}^{\bar{\boldsymbol{d}}}_{\dot{\boldsymbol{E}}}\right):\dot{\boldsymbol{E}} \tag{34}$$

where the geometric mapping tensor $\mathbb{M}^{\bar{\boldsymbol{d}}}_{\dot{\boldsymbol{E}}} = \mathbb{M}^{\bar{\boldsymbol{d}}}_{\dot{\boldsymbol{A}}}:\mathbb{M}^{\dot{\boldsymbol{A}}}_{\dot{\boldsymbol{E}}}$ obtained from the spectral forms of $\mathbb{M}^{\bar{\boldsymbol{d}}}_{\dot{\boldsymbol{A}}}$ and $\mathbb{M}^{\dot{\boldsymbol{A}}}_{\dot{\boldsymbol{E}}}$ is

$$\mathbb{M}^{\bar{\boldsymbol{d}}}_{\dot{\boldsymbol{E}}} = \sum_{i=1}^{3}\boldsymbol{M}_i\otimes\boldsymbol{M}_i + \\ + \sum_{i=1}^{3}\sum_{j\neq i}\frac{\lambda_j^2 - \lambda_i^2}{2\lambda_i\lambda_j\left(\ln\lambda_j - \ln\lambda_i\right)}\;\boldsymbol{M}^S_{ij}\otimes\boldsymbol{M}^S_{ij} \tag{35}$$

with

$$\lim_{\lambda_j\to\lambda_i}\frac{\lambda_j^2 - \lambda_i^2}{2\lambda_i\lambda_j\left(\ln\lambda_j - \ln\lambda_i\right)} = 1 \tag{36}$$

The comparison of Eqs. (30) and (34) provides

$$\boldsymbol{T} = \bar{\boldsymbol{\tau}}:\mathbb{M}^{\bar{\boldsymbol{d}}}_{\dot{\boldsymbol{E}}} = \mathbb{M}^{\bar{\boldsymbol{d}}}_{\dot{\boldsymbol{E}}}:\bar{\boldsymbol{\tau}} \tag{37}$$

Finally, projecting $\boldsymbol{T}$ and $\bar{\boldsymbol{\tau}}$ in the principal material strain directions $\boldsymbol{N}_i$ and combining Eqs. (35) and (37), we get the following useful relations between the components of both tensors in the Lagrangian strain basis

$$T_{ij} = \bar{\tau}_{ij} \qquad \text{if} \quad i = j$$
$$\tag{38}$$
$$T_{ij} = \frac{\lambda_j^2 - \lambda_i^2}{2\lambda_i\lambda_j\left(\ln\lambda_j - \ln\lambda_i\right)}\;\bar{\tau}_{ij} \text{ if } \quad i \neq j$$

2.5 Elastic tangent moduli

The model presented in Section 2.3 is well suited to be implemented in a Finite Element Analysis code. Frequently, the treatment of the incompressible hyperelastic model is based on a penalty method in which a relatively high volumetric stiffness contribution is added to the isochoric strain energy function given in Eq. (18), providing a behavior that can be considered as slightly compressible. The value assigned to the penalty parameter will determine the accuracy of the results in terms of incompressibility.

To this end, the logarithmic strain tensor $\boldsymbol{E}$ is split into its (additive) isochoric and volumetric parts

$$\boldsymbol{E} = \boldsymbol{E}^{iso} + \boldsymbol{E}^{vol} \tag{39}$$

$$\boldsymbol{E}^{vol} = \frac{1}{3}\left(\ln J\right)\boldsymbol{I} = \frac{1}{3}\left(tr\boldsymbol{E}\right)\boldsymbol{I} = \frac{1}{3}\left(\boldsymbol{E}:\boldsymbol{I}\right)\boldsymbol{I} \tag{40}$$

$$\boldsymbol{E}^{iso} = \boldsymbol{E} - \boldsymbol{E}^{vol} = \left(\mathbb{I}^S - \frac{1}{3}\boldsymbol{I}\otimes\boldsymbol{I}\right):\boldsymbol{E} = \mathbb{P}^S:\boldsymbol{E} \tag{41}$$

where $J = \det(\boldsymbol{X})$ and $\mathbb{I}^S_{ijkl} = 1/2\left(\delta_{ik}\delta_{jl} + \delta_{il}\delta_{jk}\right)$ is the fourth-order identity tensor with minor and major symmetries. The deviatoric projector tensor $\mathbb{P}^S = \mathbb{I}^S - 1/3\left(\boldsymbol{I}\otimes\boldsymbol{I}\right)$, defined in terms of full symmetric tensors $\mathbb{I}^S$ and $\boldsymbol{I}\otimes\boldsymbol{I}$, preserves the symmetries. The stored energy function, represented by $\Psi\left(\boldsymbol{E}\right)$, is then written as

$$\Psi\left(\boldsymbol{E}\right) = \mathcal{W}\left(\boldsymbol{E}^{iso},\boldsymbol{a}_0,\boldsymbol{b}_0\right) + \mathcal{U}\left(J\right) \tag{42}$$

where $\mathcal{W}(\boldsymbol{E}^{iso},\boldsymbol{a}_0,\boldsymbol{b}_0)$, as given in Eq. (18), represents the pure isochoric contribution to the strain energy and $\mathcal{U}\left(J\right)$, for which a typical explicit form is given in the examples below, represents the pure volumetric contribution to $\Psi\left(\boldsymbol{E}\right)$.

Using the additive decomposition of Eq. (42), the Generalized Kirchhoff stress tensor $\boldsymbol{T} = \partial\Psi/\partial\boldsymbol{E}$ can be calculated as $\boldsymbol{T} = \boldsymbol{T}^{iso} + \boldsymbol{T}^{vol}$, with

$$\boldsymbol{T}^{iso} = \frac{\partial\mathcal{W}}{\partial\boldsymbol{E}} = \frac{\partial\mathcal{W}}{\partial\boldsymbol{E}^{iso}}:\frac{\partial\boldsymbol{E}^{iso}}{\partial\boldsymbol{E}} = \frac{\partial\mathcal{W}}{\partial\boldsymbol{E}^{iso}}:\mathbb{P}^S \tag{43}$$

$$\boldsymbol{T}^{vol} = \frac{\partial\mathcal{U}}{\partial\boldsymbol{E}} = \frac{\partial\mathcal{U}}{\partial J}\frac{\partial J}{\partial\left(\ln J\right)}\frac{\partial\left(\ln J\right)}{\partial\boldsymbol{E}} = J\frac{d\mathcal{U}}{dJ}\boldsymbol{I} \tag{44}$$

The specific form of the strain energy Eq. (18) yields the following expression for the stress-like symmetric tensor $\partial\mathcal{W}/\partial\boldsymbol{E}^{iso}$ projected in the preferred orthotropic directions $\boldsymbol{X}_{pr} = \{\boldsymbol{e}_1,\boldsymbol{e}_2,\boldsymbol{e}_3\} = \{\boldsymbol{a}_0,\boldsymbol{b}_0,\boldsymbol{c}_0\}$

$$\frac{\partial\mathcal{W}}{\partial\boldsymbol{E}^{iso}} = \sum_{i=1}^{3}\sum_{j=1}^{3}\frac{d\omega_{ij}(E^{iso}_{ij})}{dE^{iso}_{ij}}\;\boldsymbol{L}^S_{ij} \tag{45}$$

where

$$\boldsymbol{L}^S_{ij} = \frac{1}{2}\left(\boldsymbol{e}_i\otimes\boldsymbol{e}_j + \boldsymbol{e}_j\otimes\boldsymbol{e}_i\right)$$

Note that we consider the inherent (symmetry) relations $2\omega_{ij}(E_{ij}^{iso}) = \omega_{ij}(E_{ij}^{iso}) + \omega_{ji}(E_{ji}^{iso})$ for $i \neq j$ in Eq. (18) before carrying out the differentiation $\partial \mathcal{W}/\partial \boldsymbol{E}^{iso}$.

The Second Piola Kirchhoff stress tensor is obtained from the inverse mapping of Eq. (29)

$$\boldsymbol{S} = \boldsymbol{T} : \frac{\partial \boldsymbol{E}}{\partial \boldsymbol{A}} = \frac{\partial \Psi}{\partial \boldsymbol{E}} : \frac{\partial \boldsymbol{E}}{\partial \boldsymbol{A}} \tag{46}$$

where $\partial \boldsymbol{E}/\partial \boldsymbol{A} = \mathbb{M}\dot{\overset{\boldsymbol{E}}{\boldsymbol{A}}}$. It is straightforward to obtain the spectral form of this mapping tensor using Eq. (25) and the identity $\mathbb{M}\dot{\overset{\boldsymbol{E}}{\boldsymbol{A}}}\mathbb{M}\dot{\overset{\boldsymbol{A}}{\boldsymbol{E}}} = \mathbb{I}^S$

$$\frac{\partial \boldsymbol{E}}{\partial \boldsymbol{A}} = \mathbb{M}\dot{\overset{\boldsymbol{E}}{\boldsymbol{A}}} = \sum_{i=1}^{3} \lambda_i^{-2} \, \boldsymbol{M}_i \otimes \boldsymbol{M}_i +$$
$$+ \sum_{i=1}^{3}\sum_{j\neq i} \frac{2\left(\ln \lambda_j - \ln \lambda_i\right)}{\lambda_j^2 - \lambda_i^2} \, \boldsymbol{M}_{ij}^S \otimes \boldsymbol{M}_{ij}^S \tag{47}$$

The elasticity tensor in the material description is then obtained by the formal application of the chain rule over the tensor $\boldsymbol{S}$ given in Eq. (46)

$$\mathbb{C} = \frac{\partial \boldsymbol{S}}{\partial \boldsymbol{A}} = \frac{\partial \boldsymbol{E}}{\partial \boldsymbol{A}} : \frac{\partial^2 \Psi}{\partial \boldsymbol{E}\partial \boldsymbol{E}} : \frac{\partial \boldsymbol{E}}{\partial \boldsymbol{A}} + \frac{\partial \Psi}{\partial \boldsymbol{E}} : \frac{\partial^2 \boldsymbol{E}}{\partial \boldsymbol{A}\partial \boldsymbol{A}} \tag{48}$$

which, obviously, can also be split into its isochoric and volumetric parts $\mathbb{C} = \mathbb{C}^{iso} + \mathbb{C}^{vol}$. Expressions for both $\partial \boldsymbol{E}/\partial \boldsymbol{A}$ (which major symmetry has been taken into account in Eq. (48)) and $\partial \Psi/\partial \boldsymbol{E} = \boldsymbol{T} = \boldsymbol{T}^{iso} + \boldsymbol{T}^{vol}$ have just been given above. In what follows, we provide expressions for the remaining tensors in Eq. (48), that is, the fourth-order moduli tensor $\partial^2 \Psi/\partial \boldsymbol{E}\partial \boldsymbol{E}$ and the sixth-order mapping tensor $\partial^2 \boldsymbol{E}/\partial \boldsymbol{A}\partial \boldsymbol{A}$.

The elasticity tensor $\partial^2 \Psi/\partial \boldsymbol{E}\partial \boldsymbol{E}$ is obtained from our model by means of

$$\frac{\partial^2 \Psi}{\partial \boldsymbol{E}\partial \boldsymbol{E}} = \frac{\partial \boldsymbol{T}}{\partial \boldsymbol{E}} = \frac{\partial \boldsymbol{T}^{iso}}{\partial \boldsymbol{E}} + \frac{\partial \boldsymbol{T}^{vol}}{\partial \boldsymbol{E}} \tag{49}$$

Using Eqs. (43) and (44), we get

$$\frac{\partial \boldsymbol{T}^{iso}}{\partial \boldsymbol{E}} = \frac{\partial^2 \mathcal{W}}{\partial \boldsymbol{E}\partial \boldsymbol{E}} = \mathbb{P}^S : \frac{\partial^2 \mathcal{W}}{\partial \boldsymbol{E}^{iso}\partial \boldsymbol{E}^{iso}} : \mathbb{P}^S \tag{50}$$

$$\frac{\partial \boldsymbol{T}^{vol}}{\partial \boldsymbol{E}} = \frac{\partial^2 \mathcal{U}}{\partial \boldsymbol{E}\partial \boldsymbol{E}} = \left(J\frac{d\mathcal{U}}{dJ} + J^2\frac{d^2\mathcal{U}}{dJ^2}\right) \boldsymbol{I} \otimes \boldsymbol{I} \tag{51}$$

where the second gradient tensor $\partial^2 \mathcal{W}/\partial \boldsymbol{E}^{iso}\partial \boldsymbol{E}^{iso}$ can be calculated in terms of the second derivatives of the strain energy terms ω_{ij}, i.e.

$$\frac{\partial^2 \mathcal{W}}{\partial \boldsymbol{E}^{iso}\partial \boldsymbol{E}^{iso}} = \sum_{i=1}^{3}\sum_{j=1}^{3} \frac{d^2\omega_{ij}(E_{ij}^{iso})}{(dE_{ij}^{iso})^2} \, \boldsymbol{L}_{ij}^S \otimes \boldsymbol{L}_{ij}^S \tag{52}$$

Although full symmetries are directly imposed to the tensor $\partial^2 \mathcal{W}/\partial \boldsymbol{E}^{iso}\partial \boldsymbol{E}^{iso}$ in Eq. (52) (by means of the

use of the basis tensors $\boldsymbol{L}_{ij}^S \otimes \boldsymbol{L}_{ij}^S$), note that the isochoric strain energy function given in Eq. (18) would also provide all these symmetries if its arguments were written as $E_{ij}^{iso} = (E_{ij}^{iso} + E_{ij}^{iso})/2$. However, we do not adopt this full-symmetric notation for gaining simplicity throughout the text.

The last tensorial expression we provide is that of the sixth-order purely geometrical tensor $\partial^2 \boldsymbol{E}/\partial \boldsymbol{A}\partial \boldsymbol{A}$. This is also a (geometrical) mapping tensor, which relates the rate of the mapping $\partial \boldsymbol{E}/\partial \boldsymbol{A}$ and the rate of the Green-Lagrange strain tensor $\boldsymbol{A}$, i.e.

$$\left(\dot{\overline{\frac{\partial \boldsymbol{E}}{\partial \boldsymbol{A}}}}\right) = \frac{\partial^2 \boldsymbol{E}}{\partial \boldsymbol{A}\partial \boldsymbol{A}} : \dot{\boldsymbol{A}} \tag{53}$$

This sixth-order tensor can be entirely determined following a similar procedure to that inferred from Ref. [3] (where the result for the sixth-order tensor $\partial^2 \boldsymbol{A}/\partial \boldsymbol{U}\partial \boldsymbol{U}$ is provided), that is, by means of the comparison of the spectral forms of the rates of both $\partial \boldsymbol{E}/\partial \boldsymbol{A}$ and $\boldsymbol{A}$. Alternatively, this tensor can be obtained by direct derivation, as Miehe and Lambrecht show in Ref. [25]. However, to be more concise, we only give herein the expression of the second addend of Eq. (48), i.e. $\boldsymbol{T} : (\partial^2 \boldsymbol{E}/\partial \boldsymbol{A}\partial \boldsymbol{A}) = (\partial^2 \boldsymbol{E}/\partial \boldsymbol{A}\partial \boldsymbol{A}) : \boldsymbol{T}$, which can directly (and more efficiently) be implemented in the finite elements code. Using $\boldsymbol{T} = \sum\sum T_{ij}\boldsymbol{M}_{ij}^S$, the fourth-order tensor $(\partial^2 \boldsymbol{E}/\partial \boldsymbol{A}\partial \boldsymbol{A}) : \boldsymbol{T}$ is found to be

$$\frac{\partial^2 \boldsymbol{E}}{\partial \boldsymbol{A}\partial \boldsymbol{A}} : \boldsymbol{T} = \sum_{i=1}^{3} F\left(\lambda_i\right) T_{ii} \, \boldsymbol{M}_i \otimes \boldsymbol{M}_i \tag{54}$$

$$+ \sum_{i=1}^{3}\sum_{j\neq i} G\left(\lambda_i, \lambda_j\right) T_{ii} \, \boldsymbol{M}_{ij}^S \otimes \boldsymbol{M}_{ij}^S \tag{55}$$

$$+ \sum_{i=1}^{3}\sum_{j\neq i} G\left(\lambda_i, \lambda_j\right) T_{ij} \, \mathbb{L}_{iij}^S \tag{56}$$

$$+ \sum_{i=1}^{3}\sum_{j\neq i}\sum_{j\neq k\neq i} \frac{1}{2} H\left(\lambda_i, \lambda_j, \lambda_k\right) T_{ik} \, \mathbb{L}_{ijk}^S \tag{57}$$

where

$$\mathbb{L}_{ijk}^S = \boldsymbol{M}_{ij}^S \otimes \boldsymbol{M}_{jk}^S + \boldsymbol{M}_{jk}^S \otimes \boldsymbol{M}_{ij}^S \tag{58}$$

$$F\left(\lambda_i\right) = -\frac{2}{\lambda_i^4} \tag{59}$$

$$G\left(\lambda_i, \lambda_j\right) = \frac{8\left(\log \lambda_j - \log \lambda_i\right) - 4\Lambda_{ij}/\lambda_i^2}{\Lambda_{ij}^2} \tag{60}$$

$$H\left(\lambda_i, \lambda_j, \lambda_k\right) = 8\frac{-\Lambda_{jk}\log\lambda_i - \Lambda_{ki}\log\lambda_j - \Lambda_{ij}\log\lambda_k}{\Lambda_{ij}\Lambda_{jk}\Lambda_{ki}} \tag{61}$$

with $\Lambda_{ij} = \lambda_j^2 - \lambda_i^2$. From Eq. (61), it can be seen that $H\left(\lambda_i, \lambda_j, \lambda_k\right) = H\left(\lambda_j, \lambda_i, \lambda_k\right) = H\left(\lambda_i, \lambda_k, \lambda_j\right) = H\left(\lambda_k, \lambda_j, \lambda_i\right)$. However, note that $G\left(\lambda_i, \lambda_j\right) \neq G\left(\lambda_j, \lambda_i\right)$. Also, it is straightforward to compute the special cases when two or three principal stretches converge to the same value

$$H\left(\lambda_i, \lambda_j, \lambda_k \to \lambda_i\right) = G\left(\lambda_i, \lambda_j\right) \tag{62}$$

$$H\left(\lambda_i, \lambda_j \to \lambda_i, \lambda_k \to \lambda_i\right) = G\left(\lambda_i, \lambda_j \to \lambda_i\right) = F\left(\lambda_i\right) \tag{63}$$

Using the symmetric dependences of $H\left(\lambda_i, \lambda_j, \lambda_k\right)$, other equivalent results to Eq. (62) hold. We note that each term of the summation given in Eqs. (54)–(57) presents minor and major symmetries, so the final result obtained for $\left(\partial^2 \boldsymbol{E}/\partial \boldsymbol{A}\partial \boldsymbol{A}\right) : \boldsymbol{T}$ preserves them.

Hence, as a summary, the elasticity tensor $\mathbb{C} = \mathbb{C}^{iso} + \mathbb{C}^{vol}$ is

$$\mathbb{C}^{iso} = \frac{\partial \boldsymbol{E}}{\partial \boldsymbol{A}} : \frac{\partial \boldsymbol{T}^{iso}}{\partial \boldsymbol{E}} : \frac{\partial \boldsymbol{E}}{\partial \boldsymbol{A}} + \frac{\partial^2 \boldsymbol{E}}{\partial \boldsymbol{A}\partial \boldsymbol{A}} : \boldsymbol{T}^{iso} \tag{64}$$

$$\mathbb{C}^{vol} = \frac{\partial \boldsymbol{E}}{\partial \boldsymbol{A}} : \frac{\partial \boldsymbol{T}^{vol}}{\partial \boldsymbol{E}} : \frac{\partial \boldsymbol{E}}{\partial \boldsymbol{A}} + \frac{\partial^2 \boldsymbol{E}}{\partial \boldsymbol{A}\partial \boldsymbol{A}} : \boldsymbol{T}^{vol} \tag{65}$$

where all the needed expressions to compute these tensors are provided above.

3 Strain-energy function determination from experimental data

In this section we explain the procedure to obtain the different terms that are present in the isochoric strain energy function given in Eq. (18) from experimental measures. Some of the concepts reviewed in the previous sections will be used. As mentioned above, six experimental curves are needed to entirely determine the strain energy function $\mathcal{W}$ of Eq. (18). Three of these curves will be used to calculate the axial terms ω_{ii} ($i = 1, 2, 3$) of $\mathcal{W}$ using the particular case given by Eq. (19) and the other three curves to determine the shear terms ω_{ij} ($i \neq j$).

3.1 Determination of ω_{ii} ($i = 1, 2, 3$)

The three longitudinal contributions ω_{ii} to the strain energy $\mathcal{W}$ can be obtained from several sets of experimental data points. We present here the two of them which we consider more usual and relevant.

3.1.1 Two independent uniaxial tests in two orthotropic directions

In this case, the experimental data points are obtained from two tension-compression uniaxial tests performed along two preferred directions of the material, which we choose to be the directions $\boldsymbol{e}_1$ and $\boldsymbol{e}_2$. In both cases, since the principal directions of deformation are the orthotropic material directions, all the stress and strain tensors have the same eigenvectors, i.e. $T_{ij} = \bar{\tau}_{ij} = 0$ for $i \neq j$ in Eq. (38), and hence both $\boldsymbol{T}$ and $\bar{\boldsymbol{\tau}}$ are coincident in these particular load cases. Furthermore, since the tested material is assumed to be completely incompressible, the Jacobian determinant is $J = \lambda_1\lambda_2\lambda_3 = 1$ and $\boldsymbol{T}$ is also coincident with the rotated Cauchy stress tensor $\bar{\boldsymbol{\sigma}} = \bar{\boldsymbol{\tau}}/J = \bar{\boldsymbol{\tau}}$. Obviously, there is no rotation in these deformation states, so $\boldsymbol{R} = \boldsymbol{I}$ and $\boldsymbol{\sigma} = \boldsymbol{T}$.

Then, for these purely isochoric states of deformation, in which the constraint $\boldsymbol{E} = \boldsymbol{E}^{iso}$ is enforced (note the difference with the nearly incompressible case detailed in Section 2.5), we obtain

$$\boldsymbol{\sigma} = \boldsymbol{T} = \frac{\partial \mathcal{W}}{\partial \boldsymbol{E}} + p\boldsymbol{I} \tag{66}$$

where p represents a hydrostatic pressure required to maintain incompressibility, which must be calculated by means of equilibrium equations and proper boundary conditions. In view of this last equation and of decomposition Eq. (18), the principal Cauchy stresses, measured in the reference system $\boldsymbol{X}_{pr}$, are

$$\sigma_1 = \frac{d\omega_{11}\left(E_1\right)}{dE_1} + p$$

$$\sigma_2 = \frac{d\omega_{22}\left(E_2\right)}{dE_2} + p \tag{67}$$

$$\sigma_3 = \frac{d\omega_{33}\left(E_3\right)}{dE_3} + p$$

where E_1, E_2 and E_3 (principal logarithmic strains) are subjected to the incompressibility condition $E_1 + E_2 + E_3 = 0$.

In what follows, we will add the superscripts 1 or 2 to the variables measured in (or associated to) the tests performed in direction $\boldsymbol{e}_1$ or $\boldsymbol{e}_2$, respectively. The measures (pairs) to be taken from the uniaxial test in direction $\boldsymbol{e}_1$ are the axial strain-stress data points $\{\tilde{E}_1^1, \tilde{\sigma}_1^1\}$ and the longitudinal-transverse strains $\{\tilde{E}_1^1, \tilde{E}_2^1\}$. From the second test, the strain-stress data points $\{\tilde{E}_2^2, \tilde{\sigma}_2^2\}$ are required only. The tilde decoration is used to denote discrete data values associated to the tests. In the case of infinitesimal linear orthotropic elasticity, these

experimental data points would yield the Young's modulus E_{Y_1} and the Poisson's ratio ν_{12} from the first uniaxial test and the Young's modulus E_{Y_2} from the second test. Due to the incompressible behavior, the remaining Young's modulus and Poisson's ratios are no longer arbitrary and would be easily calculated in terms of these three independent material constants obtained from the experiments (the corresponding relationships are detailed in Section 4.1).

For the general case, Eqs. (67) yield for the test in direction $\boldsymbol{e}_1$

$$\tilde{\sigma}_1^1(\tilde{E}_1^1) = \left.\frac{d\omega_{11}(E_1)}{dE_1}\right|_{\tilde{E}_1^1} + p$$

$$0 = \left.\frac{d\omega_{22}(E_2)}{dE_2}\right|_{\tilde{E}_2^1} + p \qquad (68)$$

$$0 = \left.\frac{d\omega_{33}(E_3)}{dE_3}\right|_{\tilde{E}_3^1} + p$$

where the normal Cauchy stresses in both transversal directions have been made equal to zero and the transverse strains in direction $\boldsymbol{e}_3$ are

$$\tilde{E}_3^1 = -\tilde{E}_1^1 - \tilde{E}_2^1 \qquad (69)$$

which are known values obtained from the incompressibility constraint $\tilde{E}_1^1 + \tilde{E}_2^1 + \tilde{E}_3^1 = 0$. Factoring out the pressure from Eqs. (68), they can be rewritten as

$$\tilde{\sigma}_1^1(\tilde{E}_1^1) = \omega_{11}'(\tilde{E}_1^1) - \omega_{22}'(\tilde{E}_2^1) \qquad (70)$$

$$\omega_{22}'(\tilde{E}_2^1) = \omega_{33}'(\tilde{E}_3^1) \qquad (71)$$

For the test in direction $\boldsymbol{e}_2$, proceeding in the same way as before, the corresponding equilibrium equations are

$$\tilde{\sigma}_2^2(\tilde{E}_2^2) = \omega_{22}'(\tilde{E}_2^2) - \omega_{11}'(\tilde{E}_1^2) \qquad (72)$$

$$\omega_{11}'(\tilde{E}_1^2) = \omega_{33}'(\tilde{E}_3^2) \qquad (73)$$

where in this occasion, unlike the test in direction $\boldsymbol{e}_1$, the transverse strains $\tilde{E}_2^2$ and $\tilde{E}_3^2$ remain undetermined. However, they are restricted to $\tilde{E}_1^2 + \tilde{E}_2^2 + \tilde{E}_3^2 = 0$.

Finally, if we want our model to reproduce the third possible uniaxial test performed on the material, i.e. in direction $\boldsymbol{e}_3$, the compatibility equation corresponding to this hypothetical test has to be considered, that is

$$\omega_{11}'(\tilde{E}_1^3) = \omega_{22}'(\tilde{E}_2^3) \qquad (74)$$

in which, again, the transverse strains $\tilde{E}_1^3$ and $\tilde{E}_2^3$ are unknown, although they relate through $\tilde{E}_1^3 + \tilde{E}_2^3 + \tilde{E}_3^3 = 0$. Without loss of generality, the values of the longitudinal strains for this third uniaxial test may be taken to be $\tilde{E}_3^3 = \tilde{E}_1^1$. Note that the equilibrium equation in

direction $\boldsymbol{e}_3$ is not needed in this case because $\tilde{\sigma}_3^3(\tilde{E}_3^3)$ is assumed to be unknown. The strain-stress distribution $\tilde{\sigma}_3^3(\tilde{E}_3^3)$ is to be predicted by the model once the first derivative functions ω_{11}', ω_{22}' and ω_{33}' are obtained by means of the "best" fulfilling (in a least-squares sense) of Eqs. (70)–(74). The computational procedure is as follows.

First of all, the discrete distributions of experimental points $\tilde{\sigma}_1^1(\tilde{E}_1^1)$, $\tilde{E}_2^1(\tilde{E}_1^1)$ and $\tilde{\sigma}_2^2(\tilde{E}_2^2)$ are interpolated using non-uniform piecewise cubic splines (cf. Section 2.1), which we denote as $\sigma_1^1(E_1^1)$, $E_2^1(E_1^1)$ and $\sigma_2^2(E_2^2)$, respectively. Then, to increase numerical efficiency when the spline-based functions are evaluated during the finite element computations, the domains $[\tilde{E}_{1min}^1, \tilde{E}_{1max}^1]$, $[\tilde{E}_{2min}^2, \tilde{E}_{2max}^2]$ and $[\tilde{E}_{3min}^3, \tilde{E}_{3max}^3]$ are divided into N_1, N_2 and N_3 uniform intervals, which define the new $N_1 + 1$, $N_2 + 1$ and $N_3 + 1$ points of $\bar{E}_1^1$, $\bar{E}_2^2$ and $\bar{E}_3^3$, respectively (note the bar decoration to emphasize the new strain discrete distributions). Second, we assume specific distributions (with their associated spline-based representations) of the transverse strains for the real second test, $\hat{E}_1^2(E_2^2)$, and the hypothetical third test, $\hat{E}_1^3(E_3^3)$, depending on a finite number of unknown parameters, which will be determined as a part of the final solution. The hat decoration will be used to indicate that a variable is being assumed or that a function is calculated using an assumed distribution. For example, the linear dependences $\hat{E}_1^2 = -\hat{\nu}_{21}E_2^2$ and $\hat{E}_1^3 = -\hat{\nu}_{31}E_3^3$ may be proposed, $\hat{\nu}_{21}$ and $\hat{\nu}_{31}$ being constant Poisson's ratios defined within the logarithmic strain space. The remaining transverse strains may be obtained by means of the incompressibility conditions.

Then, in a similar way as we did in Ref. [21], we combine Eqs. (70) and (74) to arrive at an equation which adopts the specific form of Eq. (10), i.e.

$$\sigma_1^1(\bar{E}_1^1) = \hat{\omega}_{11}'(\bar{E}_1^1) - \hat{\omega}_{11}'(\hat{y}(\bar{E}_1^1)) \qquad (75)$$

which solution for each point $\bar{E}_1^1$ may be expressed as in Eq. (16)

$$\hat{\omega}_{11}'(\bar{E}_1^1) = \sum_{k=0}^{\infty} \sigma_1^1\left(\hat{y}^{(k)}\left(\bar{E}_1^1\right)\right) \qquad (76)$$

and calculated within any desired accuracy. In the previous two equations, the function $\hat{y}(E_1^1) = \hat{E}_1^3(E_2^1(E_1^1))$ is the composite function which results from the insertion of the spline function $E_2^1(E_1^1)$, known from the first test, as the argument of the spline function $\hat{E}_1^3(\hat{E}_2^3)$, assumed from the third one. As explained above, the mathematical constraint $\left|\hat{y}(E_1^1)\right| < \left|E_1^1\right|$ must be satisfied so that the summation (76) converges to a finite value for each strain $\hat{E}_1^1$. Most orthotropic materials fulfill this requirement. However, if Eq. (76) is non-convergent due to this reason, it can be shown that

this other inversion formula may be applied for those particular cases

$$\hat{\omega}'_{11}(\bar{E}_1^1) = -\sum_{k=1}^{\infty} \sigma_1^1 \left(\hat{h}^{(k)} \left(\bar{E}_1^1 \right) \right) \qquad (77)$$

where $\hat{h}(x)$ represents the inverse function of $\hat{y}(x)$, i.e. $\hat{h}(x) = \hat{y}^{-1}(x)$.

Subsequently, from the $N_1 + 1$ values $\hat{\omega}'_{11}(\bar{E}_1^1)$, the construction of the corresponding piecewise spline function $\hat{\omega}'_{11}(E_1)$ is carried out. Then, Eq. (72) provides the $N_2 + 1$ values

$$\hat{\omega}'_{22}(\bar{E}_2^2) = \sigma_2^2(\bar{E}_2^2) - \hat{\omega}'_{11}(\hat{E}_1^2(\bar{E}_2^2)) \qquad (78)$$

where the splines $\hat{E}_1^2(E_2^2)$, $\hat{\omega}'_{11}(E_1)$ and $\sigma_2^2(E_2^2)$ are to be used. The spline-based function $\hat{\omega}'_{22}(E_2)$ can be built using the $N_2 + 1$ computed values $\hat{\omega}'_{22}(\bar{E}_2^2)$. At this point, only the function $\hat{\omega}'_{33}$ remains to be determined. This function can be obtained, for example, from Eq. (71)

$$\hat{\omega}'_{33}(E_3^1(\bar{E}_1^1)) = \hat{\omega}'_{22}(E_2^1(\bar{E}_1^1)) \qquad (79)$$

This last equation evaluated at the $N_1 + 1$ points $\bar{E}_1^1$ provides $N_1 + 1$ values $\hat{\omega}'_{33}(\bar{E}_3^1)$, which can be interpolated to give the remaining piecewise spline function $\hat{\omega}'_{33}(E_3)$ as a result, restricted to the given interval $[\tilde{E}_{1min}^3, \tilde{E}_{1max}^3]$.

Once the three first derivative functions $\hat{\omega}'_{11}(E_1)$, $\hat{\omega}'_{22}(E_2)$ and $\hat{\omega}'_{33}(E_3)$ corresponding to the assumed distributions $\hat{E}_1^2(E_2^2)$ and $\hat{E}_1^3(E_3^3)$ have been calculated using Eqs. (70)–(72), the error associated to the fulfillment of Eqs. (73) and (74) (note that Eq. (74) has been used to be inserted in Eq. (70) but then it has not been enforced) can be computed as

$$err_2(\bar{E}_2^2) = \hat{\omega}'_{11} \left(\hat{E}_1^2(\bar{E}_2^2) \right) - \hat{\omega}'_{33} \left(\hat{E}_3^2(\bar{E}_2^2) \right) \qquad (80)$$

$$err_3(\bar{E}_3^3) = \hat{\omega}'_{11} \left(\hat{E}_1^3(\bar{E}_3^3) \right) - \hat{\omega}'_{22} \left(\hat{E}_2^3(\bar{E}_3^3) \right) \qquad (81)$$

and evaluated for the $N_2 + 1$ and $N_3 + 1$ strain values $\bar{E}_2^2$ and $\bar{E}_3^3$. Hence, the value of the parameters which define the distributions $\hat{E}_1^2(E_2^2)$ and $\hat{E}_1^3(E_3^3)$ and that minimize the objective function

$$\hat{S} = \sum_{i=1}^{N_2+1} (err_2(i))^2 + \sum_{j=1}^{N_3+1} (err_3(j))^2 \qquad (82)$$

will provide the best approximated solution (in a least-squares sense and within the space defined by the chosen form for the assumed transverse strain distributions) of the governing Eqs. (70)–(74). Note that only in this last equation the superindex 2 represents a power of order two. In order to compute optimum values for Eq. (82), we have used the Gauss-Newton procedure, which

converged in very few iterations. The initial guess was obtained from initial (infinitesimal) equivalent Poisson values. In our numerical tests, the same minimum was always obtained using other initial guesses in a rather wide window centered in the mentioned values. However, we note that it is possible to obtain other minima far from that solution in which cases the solutions may not be so optimal in replicating the experimental data. Furthermore, we note that Eq. (82) is a compromise we took in fulfilling the system of equations, but there are many other possibilities as well.

Table 1 summarizes the overall procedure to obtain the first derivative functions $\omega'_{11}(E_1)$, $\omega'_{22}(E_2)$ and $\omega'_{33}(E_3)$.

It is possible that some spline-based functions defined in this section were needed to be evaluated beyond their lower and/or upper abscissa limits. In these cases, the spline functions may be extrapolated in order to obtain the required values. These (linear, quadratic or cubic) extrapolations should be considered during both the spline function determination (Table 1) and the later Finite Element Analysis.

3.1.2 Three independent uniaxial tests in the three preferred directions

In this case, the experimental data points are obtained from three tension-compression uniaxial tests performed along the three preferred directions of the material, i.e. e_1, e_2 and e_3. The required experimental distributions are the respective axial strain-stress data points $\{\tilde{E}_1^1, \tilde{\sigma}_1^1\}$, $\{\tilde{E}_2^2, \tilde{\sigma}_2^2\}$ and $\{\tilde{E}_3^3, \tilde{\sigma}_3^3\}$. Note that these experimental data measures are equivalent to provide the three independent Young's moduli E_{Y_1}, E_{Y_2} and E_{Y3} within the small strain and linear elasticity context.

The governing equations for this case are the same set of equations as for the case explained in Section 3.1.1, i.e. Eqs. (70)–(74), plus the additional equilibrium equation involving the strain-stress distribution $\tilde{\sigma}_3^3(\tilde{E}_3^3)$, which was irrelevant in the previous subsection. Herein, $\tilde{\sigma}_3^3(\tilde{E}_3^3)$ is part of the initial experimental data and the following equilibrium equation must be taken into account

$$\tilde{\sigma}_3^3(\tilde{E}_3^3) = \omega'_{33}(\tilde{E}_3^3) - \omega'_{11}(\tilde{E}_1^3) \qquad (83)$$

The procedure to solve the system formed by Eqs. (70)–(74) and Eq. (83) is similar to the methodology presented in the previous subsection. The only differences are that the transverse strains for the first test will also be assumed, that $\hat{\omega}'_{33}(E_3)$ will be calculated in this occasion through Eq. (83), i.e.

$$\hat{\omega}'_{33}(\bar{E}_3^3) = \sigma_3^3(\bar{E}_3^3) - \hat{\omega}'_{11}(\hat{E}_1^3(\bar{E}_3^3)) \qquad (84)$$

Table 1 Computational procedure for the case of Section 3.1.1

Calculation of $\omega'_{11}(E_1)$, $\omega'_{22}(E_2)$, $\omega'_{33}(E_3)$. **First case.**

1. Experimental data: $\tilde{\sigma}_1^1(\tilde{E}_1^1)$, $\tilde{E}_2^1(\tilde{E}_1^1)$ and $\tilde{\sigma}_2^2(\tilde{E}_2^2)$ from two tension-compression uniaxial tests (directions $\boldsymbol{e}_1$ and $\boldsymbol{e}_2$).
2. Build (non-uniform) piecewise spline functions: $\sigma_1^1(E_1^1)$, $E_2^1(E_1^1)$ and $\sigma_2^2(E_2^2)$.
3. Assume $\tilde{E}_3^3 = \tilde{E}_1^1$ and define new $N_1 + 1$, $N_2 + 1$ and $N_3 + 1$ uniformly distributed points $\bar{E}_1^1$, $\bar{E}_2^2$ and $\bar{E}_3^3$ within their respective domains.
4. Propose two distributions $\hat{E}_1^2(E_2^2)$ and $\hat{E}_1^3(E_3^3)$ depending on several parameters that you freely specify and build the required spline functions.
5. For each strain measure $\bar{E}_1^1$, calculate $\hat{\omega}'_{11}(\bar{E}_1^1)$ with Eq.(76) (or Eq. (77)) where $\hat{y}(E_1^1)$ is composed by $\hat{E}_1^3(\hat{E}_2^3)$ and $E_2^1(E_1^1)$.
6. With all the values $\hat{\omega}'_{11}(\bar{E}_1^1)$ compute the uniform spline function $\hat{\omega}'_{11}(E_1)$.
7. Obtain $\hat{\omega}'_{22}(\bar{E}_2^2)$ and $\hat{\omega}'_{33}(\bar{E}_3^1)$ using Eqs. (78) and (79) and build the associated uniform spline functions $\omega'_{22}(E_2)$ and $\omega'_{33}(E_3)$.
8. Minimize the function Eq. (82) to find the values of the parameters which provide the best approximated solution of the Eqs. (70)–(74).

and that the objective function will be

$$\hat{S} = \sum_{i=1}^{N_1+1} (err_1(i))^2 + \sum_{j=1}^{N_2+1} (err_2(j))^2 + \sum_{k=1}^{N_3+1} (err_3(k))^2 \tag{85}$$

where

$$err_1(\bar{E}_1^1) = \hat{\omega}'_{22}\left(\hat{E}_2^1(\bar{E}_1^1)\right) - \hat{\omega}'_{33}\left(\hat{E}_3^1(\bar{E}_1^1)\right) \tag{86}$$

Hence, we directly proceed to give a step-by-step implementation in Table 2 of the overall algorithm corresponding to this case.

3.2 Determination of ω_{ij} $(i \neq j)$

In Ref. [21] we describe two different procedures to obtain a shear term of the type ω_{ij}. One method requires experimental data measures from a pure shear test and the other procedure needs input data obtained from a simple shear test. In this case, following similar steps, three simple shear tests could be used to calculate the three different functions ω_{ij} present in Eq. (18). However, because of the simplicity of this procedure, we only present herein the methodology to determine them if the experimental data are obtained from three specific pure shear tests.

Following the same lines given in Ref. [21], we show next that some specific biaxial tests performed over the orthotropic material being modelled lead to pure shear state representations for logarithmic strains in certain reference frames. We will further see that the use of

our hyperelastic model predicts associated pure shear state representations for the Cauchy stresses. Hence the determination of the first derivative functions ω'_{ij} is a very simple and direct task.

Three biaxial tests are required. In each one of them, two preferred material directions are involved. We denote the variables measured in (or associated to) the test performed in the plane defined by directions $\boldsymbol{e}_i$ and $\boldsymbol{e}_j$ with the superscript $ij = 12, 23, 31$, which in turn will provide the first derivative spline-based function ω'_{ij}. For the test ij, Figs. 1(a) and 1(b) illustrate the orientation of the reference configuration and the deformation being imposed to the material, respectively. As it can be seen, the test is performed in material (and spatial) principal strain directions $\boldsymbol{N}_i$ and $\boldsymbol{N}_j$. The direction $\boldsymbol{N}_i$ is loaded in tension and the direction $\boldsymbol{N}_j$ in compression in order to achieve the prescribed stretches $\lambda_i^{ij} > 1$ and $\lambda_j^{ij} = 1/\lambda_i^{ij}$. We consider a plane stress state in which the faces of the body normal to the direction $\boldsymbol{e}_k = \boldsymbol{N}_k$ $(i \neq k \neq j)$ are free from tractions. Note also that the preferred directions $\boldsymbol{e}_i$ and $\boldsymbol{e}_j$ are initially oriented clockwise 45° with respect to the principal strain directions $\boldsymbol{N}_i$ and $\boldsymbol{N}_j$. Then, a pure shear state for strains may be analyzed using the system of representation $\boldsymbol{X}_{pr}$, see Figures 1(c) and 1(d). The required experimental data are the measured points $(\tilde{\lambda}_i^{ij}, \tilde{\sigma}_i^{ij})$ or, equivalently, the distribution $\tilde{\sigma}_i^{ij}(\tilde{E}_i^{ij})$, where $\tilde{\sigma}_i^{ij}$ is the normal Cauchy stress acting on the face normal to $\boldsymbol{N}_i$ and $\tilde{E}_i^{ij} = \ln \tilde{\lambda}_i^{ij}$ is the axial logarithmic principal strain in that direction.

In the homogeneous deformation state depicted in Figure 1, the Hencky strain tensor $\boldsymbol{E}$ expressed in the

Table 2 Computational procedure for the case of Section 3.1.2

Calculation of $\omega'_{11}(E_1)$, $\omega'_{22}(E_2)$, $\omega'_{33}(E_3)$. **Second case.**

1. Experimental data: $\tilde{\sigma}^1_1(\tilde{E}^1_1)$, $\sigma^2_2(\tilde{E}^2_2)$ and $\tilde{\sigma}^3_3(\tilde{E}^3_3)$ from three tension-compression uniaxial tests (directions e_1, e_2 and e_3).
2. Build (non-uniform) piecewise spline functions: $\sigma^1_1(E^1_1)$, $\sigma^2_2(E^2_2)$ and $\sigma^3_3(E^3_3)$.
3. Define new $N_1 + 1$, $N_2 + 1$ and $N_3 + 1$ uniformly distributed points $\bar{E}^1_1$, $\bar{E}^2_2$ and $\bar{E}^3_3$ within their respective domains.
4. Propose three distributions $\hat{E}^1_2(E^1_1)$, $\hat{E}^2_1(E^2_2)$ and $\hat{E}^3_1(E^3_3)$ depending on several parameters that you freely specify and build the required spline functions.
5. For each strain measure $\bar{E}^1_1$, calculate $\hat{\omega}'_{11}(\bar{E}^1_1)$ with Eq.(76) (or Eq. (77)) where $\hat{y}(E^1_1)$ is composed by $\hat{E}^3_1(\hat{E}^3_3)$ and $\hat{E}^1_2(E^1_1)$.
6. With all the values $\hat{\omega}'_{11}(\bar{E}^1_1)$ compute the uniform spline function $\hat{\omega}'_{11}(E_1)$.
7. Obtain $\hat{\omega}'_{22}(\bar{E}^2_2)$ and $\hat{\omega}'_{33}(\bar{E}^3_3)$ using Eqs. (78) and (84) and build the associated uniform spline functions $\omega'_{22}(E_2)$ and $\omega'_{33}(E_3)$.
8. Minimize the function Eq. (85) to find the values of the parameters which provide the best approximated solution of Eqs. (70)–(74) and (83).
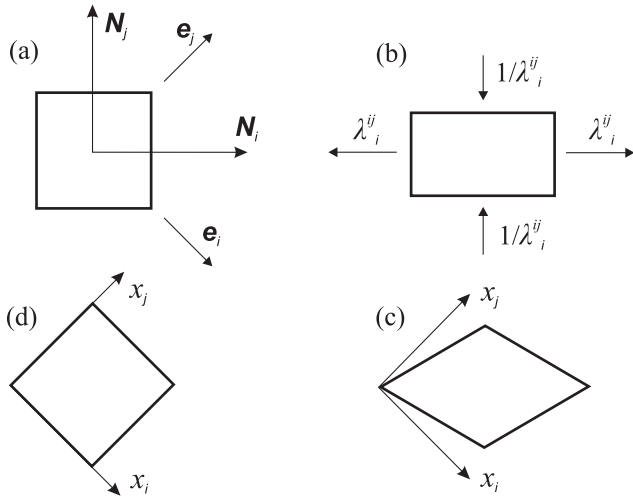
Fig. 1 Pure shear test in the plane $ij = 12, 23, 31$. From left upper corner clockwise: (a) Reference configuration represented in principal strain basis $\{N_i, N_j, N_k\}$ ($i \neq k \neq j$). (b) Kinematics of deformation in the biaxial test, with corresponding principal stretches. (c) State of deformation (pure shear state) described in material reference frame X_{pr}. (d) Reference configuration represented in X_{pr}. e_i and e_j define the orientation of the material preferred directions (clockwise 45 degrees with respect to N_i and N_j, respectively)

basis of principal stretches $\{N_i, N_j, N_k\}$ is

$$[E]_N = \ln[U]_N = \begin{bmatrix} E^{ij}_i & 0 & 0 \\ 0 & -E^{ij}_i & 0 \\ 0 & 0 & 0 \end{bmatrix} \quad (87)$$

where $E^{ij}_j = \ln\lambda^{ij}_j = \ln(1/\lambda^{ij}_i) = -E^{ij}_i$ and the result $E^{ij}_k = \ln\lambda^{ij}_k = \ln 1 = 0$ emerges as a consequence of the

isochoric motion being imposed on the plane $\{N_i, N_j\}$ and the incompressibility constraint $\lambda^{ij}_i \lambda^{ij}_j \lambda^{ij}_k = 1$. The projection of this strain tensor into the basis $X_{pr} = \{e_i, e_j, e_k\}$ provides the pure shear description

$$[E]_{X_{pr}} = \begin{bmatrix} 0 & E^{ij}_i & 0 \\ E^{ij}_i & 0 & 0 \\ 0 & 0 & 0 \end{bmatrix} \quad (88)$$

Therefore, the only non-zero component of the logarithmic strain tensor that takes part in the strain energy function given in Eq.(18) is the shear strain $E_{ij} = E^{ij}_i$.

As in the two previous subsections, the Generalized Kirchhoff stress tensor T can be obtained from

$$T = \frac{\partial \mathcal{W}}{\partial E} + pI \quad (89)$$

where the hydrostatic pressure p is found to be zero from the plane stress condition $\sigma^{ij}_k = \tau^{ij}_k = T^{ij}_k = 0$, i.e.

$$0 = \omega'_{kk}(E^{ij}_k) + p = \omega'_{kk}(0) + p = 0 + p = p \quad (90)$$

Thus, the tensor T is just

$$[T]_{X_{pr}} = \begin{bmatrix} 0 & \omega'_{ij}(E^{ij}_i) & 0 \\ \omega'_{ij}(E^{ij}_i) & 0 & 0 \\ 0 & 0 & 0 \end{bmatrix} \quad (91)$$

and a pure shear description for stresses is also obtained. Furthermore, as we mentioned above, note that this last fact implies that principal directions of strains and stresses are coincident for this specific test, so strain and stress tensors commute and T is completely coincident with σ (see Eq. 38). Then, for each strain value

$\tilde{E}_i^{ij}$, the Cauchy stress tensor in the basis of principal stretches is

$$[\boldsymbol{\sigma}]_{\boldsymbol{N}} = \begin{bmatrix} \omega'_{ij}(\tilde{E}_i^{ij}) & 0 & 0 \\ 0 & -\omega'_{ij}(\tilde{E}_i^{ij}) & 0 \\ 0 & 0 & 0 \end{bmatrix} \qquad (92)$$

where we immediately identify

$$\omega'_{ij}(\tilde{E}_i^{ij}) = \tilde{\sigma}_i^{ij}(\tilde{E}_i^{ij}) \qquad (93)$$

and, as a result, we also deduce that the stress in direction $\boldsymbol{N}_j$ predicted by our model is $\sigma_j^{ij} = -\sigma_i^{ij}$. Finally, from all the values $\omega'_{ij}(\tilde{E}_i^{ij})$, the spline representation $\omega'_{ij}(E_{ij})$ can be built.

For convenience, the procedure to determine the spline-based function $\omega'_{ij}(E_{ij})$ from each one of the three tests $ij = 12, 23, 31$ is summarized in Table 3. Unlike the previous cases, where tension and compression data points were necessary, we only need here experimental data points for $E_i^{ij} > 0$. In this case, symmetry considerations are taken into account before constructing the odd spline function of the strains $\omega'_{ij}(E_{ij})$ and the calculation $\tilde{\sigma}_i^{ij}(-\tilde{E}_i^{ij}) = -\tilde{\sigma}_i^{ij}(\tilde{E}_i^{ij})$ is performed for every strain $\tilde{E}_i^{ij} > 0$.

4 Examples

4.1 Case of linear logarithmic stress-strain measures

In this simple example we show that the incompressible orthotropic model separable in terms of uncoupled logarithmic strains Eq. (18) provides exact results for hyperelastic materials with linear logarithmic strain-stress relations. This example also illustrates that, for linear small strains, the strain energy function Eq. (18) coincides with the isochoric stored energy function of orthotropic materials undergoing infinitesimal deformations. Hence, the more general spline-based orthotropic model presented in this paper can be considered as an extension of this simple case in which general material non-linearities and finite deformations may be fully included.

For the case of linear logarithmic strain-stress relations, the strain energy function given in Eq. (18) is a quadratic function of the isochoric logarithmic strain components E_{ij}^{iso} $(i, j = 1, 2, 3)$ in the reference frame X_{pr} and it adopts the form

$$\mathcal{W} = \frac{1}{2}\left(2\mu_{11}\left(E_{11}^{iso}\right)^2 + 2\mu_{22}\left(E_{22}^{iso}\right)^2 + 2\mu_{33}\left(E_{33}^{iso}\right)^2\right)$$
$$+ 2\mu_{12}\left(E_{12}^{iso}\right)^2 + 2\mu_{23}\left(E_{23}^{iso}\right)^2 + 2\mu_{31}\left(E_{31}^{iso}\right)^2 \qquad (94)$$

where it can be identified $\omega_{ij}(E_{ij}^{iso}) = (1/2) \cdot 2\mu_{ij} \cdot (E_{ij}^{iso})^2$. Equation (94) is the extension to large strains of the infinitesimal model

$$\mathcal{W} = \frac{1}{2}\left(2\mu_{11}\left(\varepsilon_{11}^{iso}\right)^2 + 2\mu_{22}\left(\varepsilon_{22}^{iso}\right)^2 + 2\mu_{33}\left(\varepsilon_{33}^{iso}\right)^2\right)$$
$$+ 2\mu_{12}\left(\varepsilon_{12}^{iso}\right)^2 + 2\mu_{23}\left(\varepsilon_{23}^{iso}\right)^2 + 2\mu_{31}\left(\varepsilon_{31}^{iso}\right)^2 \qquad (95)$$

Here, the use of logarithmic strains is a natural extension of the use of infinitesimal strains [22]. It has been shown that using small strain constants and logarithmic strains substituting engineering strains yield a rather accurate description of the material behavior in metals up to moderate large strains [26], [27]. Furthermore, the uncoupled stored energy function is also exact in this case for large strains. Hence it has been extensively used in large strain computational plasticity [4], [5]. In Eq. (94), the unknown constants μ_{ij} stand for the six independent Lame's moduli of the purely incompressible orthotropic material under study. Again, note that symmetries of the type $2\mu_{12}(E_{12}^{iso})^2 = (2\mu_{12}(E_{12}^{iso})^2 + 2\mu_{21}(E_{21}^{iso})^2)/2$ are implicit in Eq. (94). As it is explained above, these constants are to be determined from six independent experimental curves: the first three constants (slopes) from three curves obtained from uniaxial testing (Sections 3.1.1 or 3.1.2) and the last three constants from three pure shear tests (Section 3.2) or also by means of simple shear or biaxial testing. Then, the correspondence to the small strain case is apparent.

For example, the experimental data for Section 3.1.2 would consist in these three linear relations

$$\tilde{\sigma}_i^i = E_{Y_i}\tilde{E}_i^i \qquad i = 1, 2, 3 \qquad (96)$$

where E_{Y_i} stands for the Young's modulus in the i direction. For this case, since all the functions present in the equilibrium equation of each uniaxial test are linear (see Eq. (75)), they can be solved analytically

$$\sigma_i^i(E_i^i) = 2\mu_{ii}E_i^i - 2\mu_{ii}\left[\frac{\nu_{ki}}{\nu_{kj}}(-\nu_{ij}E_i^i)\right] \qquad \epsilon_{ijk} = 1 \qquad (97)$$

$$E_{Y_i}E_i^i = 2\mu_{ii}\left(1 + \frac{\nu_{ij}\nu_{ki}}{\nu_{kj}}\right)E_i^i \qquad \epsilon_{ijk} = 1 \qquad (98)$$

to give

$$2\mu_{ii} = \frac{E_{Y_i}}{1 + \frac{\nu_{ij}\nu_{ki}}{\nu_{kj}}} \qquad \epsilon_{ijk} = 1 \qquad (99)$$

where $\epsilon_{ijk} = (\boldsymbol{e}_i \times \boldsymbol{e}_j) \cdot \boldsymbol{e}_k$ represents the permutation symbol. Using these expressions for μ_{ii}, $i = 1, 2, 3$,

Table 3 Computational procedure for the case of Section 3.2

> **Calculation of** $\omega'_{ij}(E_{ij})$ $(ij = 12, 23, 31)$
>
> 1. Experimental data: $\tilde{\sigma}_i^{ij}(\tilde{E}_i^{ij})$ from a biaxial test like the one shown in Figs. 1(a) and 1(b).
> 2. Perform the operation $\tilde{\sigma}_i^{ij}(-\tilde{E}_i^{ij}) = -\tilde{\sigma}_i^{ij}(\tilde{E}_i^{ij})$ for each value $\tilde{E}_i^{ij} > 0$.
> 3. Build (non-uniform) piecewise spline function $\sigma_i^{ij}(E_i^{ij})$ from points $\tilde{\sigma}_i^{ij}(\tilde{E}_i^{ij})$.
> 4. Define new N^{ij} subintervals with $N^{ij} + 1$ uniformly distributed points $\bar{E}_i^{ij}$.
> 5. Calculate the value $\omega'_{ij}(\bar{E}_i^{ij}) = \sigma_i^{ij}(\bar{E}_i^{ij})$ for all the strain points $\bar{E}_i^{ij}$.
> 6. Build uniform spline function $\omega'_{ij}(E_{ij})$ from all the values $\omega'_{ij}(\bar{E}_i^{ij})$.

together with the incompressibility conditions $\nu_{ij} = 1 - \nu_{ik}$, $i \neq j \neq k \neq i$, the three compatibility relations Eq. (71), Eq. (73) and Eq. (74) can be solved to provide the following values of the Poisson's ratios in terms of the Young's moduli (an expected result due to incompressibility)

$$\nu_{ij} = \frac{1}{2}E_{Yi}\left(\frac{1}{E_{Yj}} + \frac{1}{E_{Yi}} - \frac{1}{E_{Yk}}\right) \tag{100}$$
$$i \neq j \neq k \neq i = 1, 2, 3$$

These expressions are in concordance with the expressions given in Ref. [14] for infinitesimal strains, where the index numeration of the Poisson's ratios is inverted with respect to the one presented herein. Hence, using Eqs. (99) and (100), it is clear that we obtain the three longitudinal Lame constants μ_{ii} as functions of the three independent Young moduli E_{Yi}.

On the other hand, the necessary experimental data for Section 3.2 would consist in these other three linear relations

$$\tilde{\sigma}_i^{ij} = 2G_{ij}\tilde{E}_i^{ij} \qquad ij = 12, 23, 31 \tag{101}$$

where G_{ij} is the elastic shear moduli corresponding to the test performed in the ij plane. Then, from Eq. (93), we get

$$\mu_{ij} = G_{ij} \qquad ij = 12, 23, 31 \tag{102}$$

where the correspondence with the small strain case is again apparent.

Once the six independent material parameters characterizing the purely incompressible material are known from experimental testing, the deviatoric strain energy function Eq. (94) formed by uncoupled additive terms can be used to exactly predict the stress field associated to a general finite deformation state undergone by this type of materials. That is, in a similar way to what occurs in the small strain case, the constitutive behavior does not depend on the coupled term $E_{12}E_{23}E_{31}$ (see Eq. 17) and the quadratic strain energy function given

in Eq. (94) is exact. Moreover, in the following Sections we show that for the more general, non-linear, case the consideration of the six functions present in Eq. (18) is sufficient to very accurately predict the mechanical behavior of the material in six different, independent, experimental tests. Hence, because of these two last reasons, we do not consider relevant for practical purposes the absence of the term depending on $E_{12}E_{23}E_{31}$ in Eq. (18).

4.2 Uniaxial tests in preferred orthotropic directions

To the best of the authors' knowledge, there is no work in the literature which contains a complete set of experimental tests performed over the same material and which provides the needed data to define the non-linear model we present in this paper (and of course none to completely define the orthotropic behavior of a material). However, for the transversely isotropic model that we recently presented in Ref. [21], we were able to completely describe the model (at least in the relevant part) using the experimental results of Morrow et al [28]. In Refs. [14], [18] (see also the references cited therein) and [29], it can be seen that a usual approach to characterize an incompressible orthotropic hyperelastic material is by means of the fitting of a set of two strain-stress curves obtained from mechanical testing. All the strain energy functions presented in those works have a predefined shape and contain several constants to be determined from the experimental data-fitting process. Other works provide experimental results obtained from specific planar biaxial tests, see for example Ref. [30], or from a set of simple shear tests, see Ref. [31], which can be used to characterize the shear response of the chosen hyperelastic model (cf. Ref. [17]). The difference between our approach and that of those references is that in our case, if the mentioned complete set of experimental test data were available for the same material, our model would be capable of "exactly" cap-

ture the behavior for all tests simultaneously, regardless of the shape of the curves. Hence, the fact that our model needs a complete set of six curves should never be considered as a drawback because some of them can be "guessed" or "assumed" without affecting the other ones. In contrast, in the previous works the remaining curves are intrinsically imposed by the model, not by the material behavior.

Then, in order to include some examples of "real" material behavior, we combine actual results obtained from experiments with other assumed "experimental" distributions, used as input data to define the model given in Eq. (18). Although we are characterizing an incompressible orthotropic material, we use experimental data points from a transversely isotropic rubber-like material measured by Diani et al [32]. We assume herein that these two curves are associated to an orthotropic material and then proceed to perform a parametric study in terms of transverse strain distributions, following the procedure detailed in Table 1 for each case. We show how the consideration of several Poisson's ratio "experimental" values ν_{12} as input data ($\tilde{E}_2^1 = -\nu_{12}\tilde{E}_1^1$) will effectively lead to different orthotropic stored energy functions, recovering the transversely isotropic behavior of the material under study when the specific value $\nu_{12} = 1/2$ is prescribed.

We begin the parametric study of the axial terms ω_{11}, ω_{22}, ω_{33} with an equivalent Poisson's ratio value of $\nu_{12} = 0.3$. In Figure 2, the two strain-stress point distributions obtained by Diani et al from tensile tests over the rubber-like material are represented. We present the results in terms of logarithmic strains and Cauchy stresses. Due to the absence of experimental data for the compression branch, the antisymmetric stress distributions $\tilde{\sigma}_i^i(-\tilde{E}_i^i) = -\tilde{\sigma}_i^i(\tilde{E}_i^i)$, for $i = 1, 2$ and $\tilde{E}_i^i > 0$, are assumed. If real measured compression data points were available, they could be used instead to compute the terms ω_{11}, ω_{22}, ω_{33}. In Figure 2, we also represent the predictions provided by the first derivative spline-based functions ω_{11}', ω_{22}', ω_{33}' and the Poisson's ratios ν_{21}, ν_{31} which are solution of the procedure of Table 1. These predicted stress values are calculated through

$$\sigma_1^1(\bar{E}_1^1) = \omega_{11}'(\bar{E}_1^1) - \omega_{33}'(-\nu_{13}\bar{E}_1^1) \tag{103}$$

$$\sigma_2^2(\bar{E}_2^2) = \omega_{22}'(\bar{E}_2^2) - \omega_{33}'(-\nu_{23}\bar{E}_2^2) \tag{104}$$

where $\nu_{13} = 1 - \nu_{12} = 0.7$ is directly obtained from the initially prescribed Poisson's ratio $\nu_{12} = 0.3$ and the value $\nu_{23} = 1 - \nu_{21} = 0.740$ is calculated using the computed value $\nu_{21} = 0.260$.

The strain-stress curve predicted by the model for an hypothetical uniaxial test in direction $\boldsymbol{e}_3$

$$\sigma_3^3(\bar{E}_3^3) = \omega_{33}'(\bar{E}_3^3) - \omega_{11}'(-\nu_{31}\bar{E}_1^1) \tag{105}$$
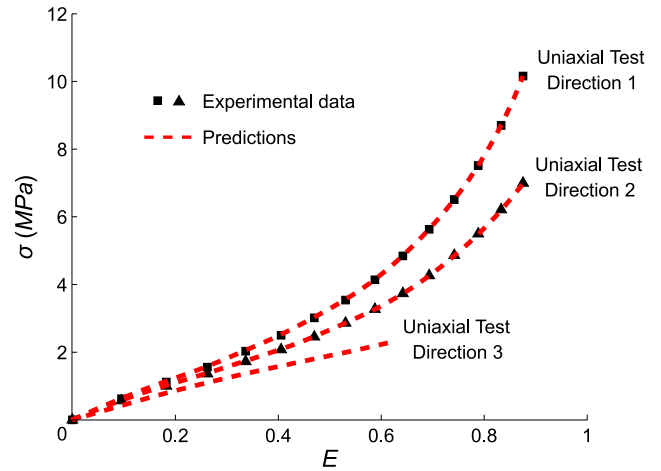

Fig. 2 Cauchy stresses $\tilde{\sigma}_1^1(\tilde{E}_1^1)$ and $\tilde{\sigma}_2^2(\tilde{E}_2^2)$ obtained from uniaxial tests performed on calendered rubber (adapted from Ref. [32]). Predictions of the experimental data (Eqs. (103) and (104)) and of an hypothetical uniaxial test in the material preferred direction 3 (Eq. (105)) using the Spline model (Section 3.1.1) with an initially prescribed transverse strain distribution $\tilde{E}_2^1 = -0.3\tilde{E}_1^1$. The material is assumed to be orthotropic for this parametric study
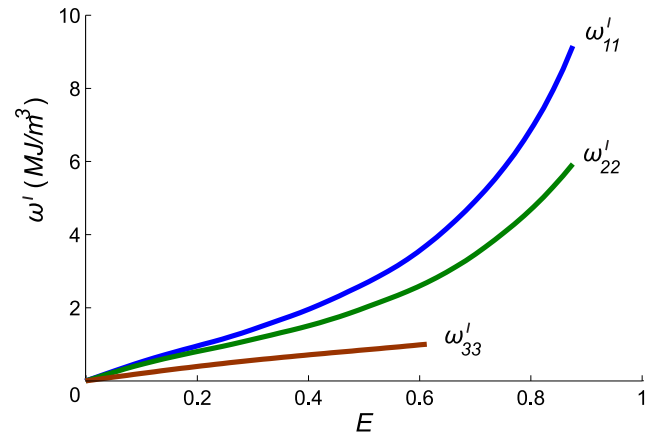

Fig. 3 Spline-based representation of the first derivative of the strain energy terms ω_{ii} ($i = 1, 2, 3$) calculated using the Spline model (Section 3.1.1) with the experimental data from Fig. 2 (or Fig. 4) and the transverse strain distribution $\tilde{E}_2^1 = -0.3\tilde{E}_1^1$

is also depicted in Figure 2. Since $\sigma_2^2(E) > \sigma_3^3(E)$ for a given $E > 0$, the material results to be stiffer in direction $\boldsymbol{e}_2$ than in direction $\boldsymbol{e}_3$ ($\omega_{22}'(E) > \omega_{33}'(E)$ as well). However, note that this is an expected result due to the fact that the specific "experimental" value $\nu_{12} < 0.5$ (and $\nu_{13} = 1 - \nu_{12} > 0.5$) has been prescribed as input data to compute the spline-based stored energy function. Clearly, the background on the small strain case is useful herein to understand the behavior of the material undergoing finite deformations, which is a clear advantage of this model. Moreover, this result shows that the calculated strain energy function captures the im-
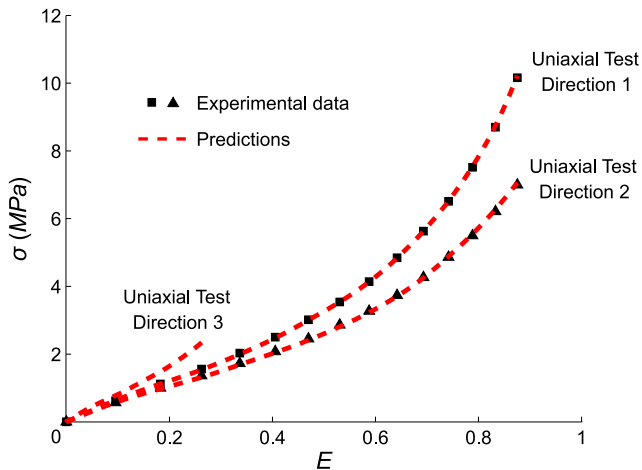
Fig. 4 Cauchy stresses $\tilde{\sigma}_1^1(\tilde{E}_1^1)$ and $\tilde{\sigma}_2^2(\tilde{E}_2^2)$ obtained from uniaxial tests performed on calendered rubber (adapted from Ref. [32]). Predictions of the experimental data (Eqs. (103) and (104)) and of an hypothetical uniaxial test in the material preferred direction 3 (Eq. (105)) using the Spline model (Section 3.1.1) with an initially prescribed transverse strain distribution $\tilde{E}_2^1 = -0.7\tilde{E}_1^1$. The material is assumed to be orthotropic for this parametric study

Fig. 5 Spline-based representation of the first derivative of the strain energy terms ω_{ii} $(i = 1, 2, 3)$ calculated using the Spline model (Section 3.1.1) with the experimental data from Fig. 4 (or Fig. 2) and the transverse strain distribution $\tilde{E}_2^1 = -0.7\tilde{E}_1^1$

portant, inherent in the experiments, information contained in the third curve and that the model provides mechanical responses in generic situations which are consistent with the experimental data.

Using the same two strain-stress point distributions obtained by Diani et al, we prescribe now a Poisson's ratio value of $\nu_{12} = 0.7$. That is, the third curve defining the in-axis behavior of the material is changed with respect to the previous example. In Figure 4 it can be seen that the model is again able to exactly predict the experimental data.

In this case, since $\nu_{12} > 0.5$ (and $\nu_{13} < 0.5$), the material is stiffer in direction 3 than in direction 2. The computed strain energy function manifest this fact, which is clear in Figures 4 and 5.

The solution values of the remaining Poisson's ratios result in $\nu_{21} = 0.623$ and $\nu_{31} = 0.408$, which are also in correspondence with the stress-strain distributions shown in Figure 4 ($\sigma_3^3(E) > \sigma_1^1(E)$ and $\sigma_1^1(E) > \sigma_2^2(E)$).

As a final case, it can be shown that for an initial value of $\nu_{12} = 1/2$ $(= \nu_{13})$, the procedure of Table 1 provides identical representations for the first derivative functions $\omega_{22}'(E)$ and $\omega_{33}'(E)$. As a result $\sigma_2^2(E) = \sigma_3^3(E) < \sigma_1^1(E)$ and the procedure converges to the case presented in Section 3.1.3 of Ref. [21], with the only exception of the index numeration. The Poisson's ratios for this case are found to be $\nu_{21} = \nu_{31} = 0.435$.

This simplistic yet useful parametric study shows the relevance of considering a third curve, additionally to $\tilde{\sigma}_1^1(\tilde{E}_1^1)$ and $\tilde{\sigma}_2^2(\tilde{E}_2^2)$, representing transverse strains
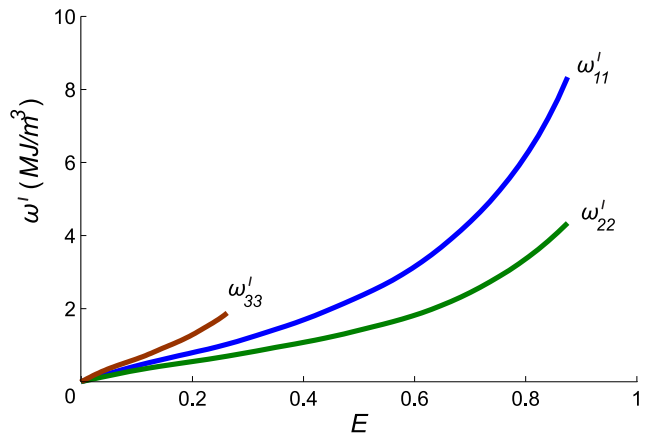
$\tilde{E}_2^1(\tilde{E}_1^1)$ or normal stresses $\tilde{\sigma}_3^3(\tilde{E}_3^3)$ to properly characterize the *longitudinal* behavior of an incompressible orthotropic material along the preferred material axes. Hence, characterizations such as the ones performed in Refs. [14] or [29], which consider only two behavior-curves obtained from uniaxial testing, are somehow incomplete and can lead to some unexpected results regarding transverse strains, as it can be seen in Ref. [16]. The importance of the third curve is apparent here.

4.3 Off-axis mechanical behavior

For deformation states in which the principal strain directions are coincident with the preferred directions of the orthotropic material (in-axis deformation), the components E_{ij}, $i \neq j$, are zero and the terms ω_{ij} are not needed to perform Finite Element simulations or any other calculations regarding these particular deformation states. When considering a more general deformation state in which the principal strain directions are not the preferred directions of the orthotropic material (off-axis deformation), the shear terms ω_{ij} must be previously calculated from experimental data. If these test results are only known for small strains, that is, the shear elastic moduli G_{ij} are known, a possible approach would be to prescribe $\tilde{\sigma}_i^{ij} = 2G_{ij}\tilde{E}_i^{ij}$, $ij = 12, 23, 31$, in the procedure of Table 3 and then to obtain a quadratic contribution for ω_{ij}. If no data is available at all (or partially), the shear curves are to be assumed, and the user of the model has to be aware of the fact that the behavior which is being prescribed will be replicated by the model.

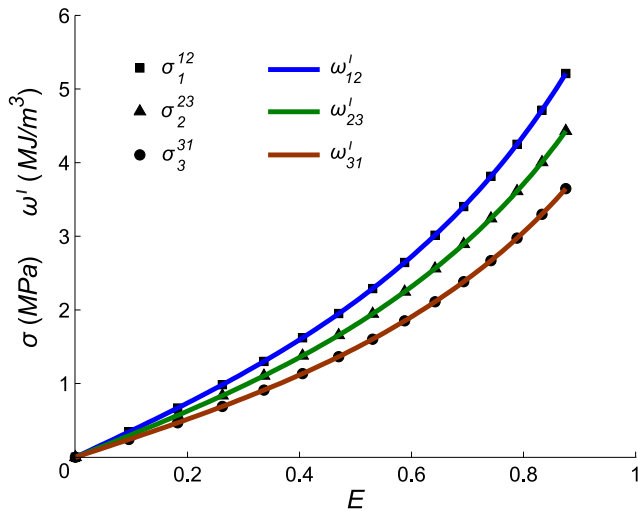To completely define our model and to reproduce the actual user situation, we will assume three pure

Fig. 6 Calculated Cauchy stress distribution $\tilde{\sigma}_1^{12}(\tilde{E}_1^{12})$ using the model of Itskov and Aksel [15] and assumed Cauchy stresses $\tilde{\sigma}_2^{23}(\tilde{E}_2^{23})$ and $\tilde{\sigma}_3^{31}(\tilde{E}_3^{31})$ for the three pure shear tests defined in Section 3.2. Spline-based representations of functions $\omega'_{12}(E_{12}) \equiv \sigma_1^{12}(E_1^{12})$, $\omega'_{23}(E_{23}) \equiv \sigma_2^{23}(E_2^{23})$ and $\omega'_{31}(E_{31}) \equiv \sigma_3^{31}(E_3^{31})$, which are solution of the procedure given in Table 3

shear test curves as detailed in Section 3.2. The prescribed "experimental" points and the direct spline-based representation of the first derivative of the strain energy function terms $\omega_{ij} \equiv \sigma_i^{ij}$ are shown in Figure 6.

In order to prescribe "experimental" results for these tests, the invariant-based transversely isotropic hyperelastic model of Itskov and Aksel of Ref. [15] has been used with the material parameters given therein, which provide the best-fit to the experimental data of Diani et al used in the previous example (cf. also Ref. [21]). Using this model, we have analytically reproduced the corresponding pure shear test of Section 3.2 to obtain the data $\tilde{\sigma}_1^{12}(\tilde{E}_1^{12})$ shown in Figure 6. The other two distributions $\tilde{\sigma}_2^{23}(\tilde{E}_2^{23})$ and $\tilde{\sigma}_3^{31}(\tilde{E}_3^{31})$ plotted in Figure 6 have been assumed to be proportional to $\tilde{\sigma}_1^{12}(\tilde{E}_1^{12})$.

In what follows, we illustrate the simulation capabilities of the present model through several numerical examples consisting in unidirectional elongations of a three-dimensional plate with a hole made of nearly incompressible orthotropic hyperelastic material. The formulation for slightly compressible materials implemented in the Finite Element code is the one presented in Section 2.5. In all solutions, fully integrated finite elements ($3 \times 3 \times 3$ Gauss integration) were used. We employ the 27-node u/p mixed formulation element (the 27/4 or Q2/P1 element) in order to prevent mesh locking [1], [33]. For the incremental analysis, a Newton–Raphson scheme is employed and asymptotic quadratic convergence is reached in each step, as should be expected due to the use of the elasticity tangent ten-

sor given in Eqs. (64)-(65). The achieved rate of convergence also manifests the fact that the spline-based representations used to build the deviatoric strain energy function Eq. (18) have the required smoothness, so they do not damage the quadratic convergence rate during the Newton–Raphson iterations. That is, each first derivative term ω'_{ij}, $i,j = 1,2,3$, is a piecewise spline function with second-order continuous derivatives, so the tangent moduli are continuously differentiable.

For the first numerical example, the employed isochoric strain energy function $\mathcal{W}$ (Eq. (18)) which contributes to the total stored energy Ψ (Eq. (42)) is formed by the three longitudinal terms ω_{ii}, $i = 1,2,3$, obtained in the previous Section for the case in which $\nu_{12} = 0.3$ and the three shear terms ω_{ij}, $i \neq j$, obtained in this Section. In Figures 3 and 6 the first derivatives of these antisymmetric functions are shown for positive strains. Recall that antisymmetry is assumed for the longitudinal terms for this particular case, whereas antisymmetry is always enforced for the shear terms. The volumetric contribution $\mathcal{U}$ to Ψ that we used in the examples is described by the well-known, simple, volumetric function

$$\mathcal{U} = \frac{1}{2}\kappa\left(J-1\right)^2 \tag{106}$$

where κ is the so-called penalty parameter (bulk modulus). To approximately enforce incompressibility, a value of $\kappa = 1000\,\text{MPa}$ has been selected to perform the simulations. We note that any other (penalty) volumetric function could be used, we employed a simple one often encountered in the literature. We refer to the work of Hartmann and Neff [34] for an analysis of some of these functions, specially regarding policonvexity of the resulting stored energy function.

A rectangular plate with a concentric circular hole (see Fig. 7) with initial length $l_0 = 32\,\text{mm}$, height $h_0 = 16\,\text{mm}$, hole radius $r_0 = 4\,\text{mm}$ and thickness $t_0 = 0.5\,\text{mm}$ is stretched under a plane strain condition along its major dimension up to a total length of $l = 44\,\text{mm}$. The finite element discretization of the plate is depicted in Fig. 7. The plate is stretched by only prescribing the horizontal displacements along the x axis at both vertical ends. The results for principal direction orientations of $\alpha = 0°$, $\alpha = 30°$, $\alpha = 60°$ and $\alpha = 90°$ are shown in Fig. 8, where α is the angle depicted in Fig. 7 between the x axis and the preferred material direction e_1. In Fig. 8, the deformed shapes and band plots of the computed deviatoric Cauchy stress norm $\left\|\sigma^{iso}\right\| = \sqrt{\sigma^{iso} : \sigma^{iso}}$ for the different orientations are depicted. We employ the tensor $\sigma^{iso} = \mathbb{P}^S : \sigma$ to directly see the influence of function $\mathcal{W}$ in the results. As it could be expected, angular distortions appear for the orientations $\alpha = 30°$ and $\alpha = 60°$ due to the off-axis

Table 4 Asymptotic quadratic convergence: Unbalanced energy and force during a typical computed step using a Newton–Raphson scheme

Step	Iteration	Force	Energy
5/6	1/4	1.000E+00	1.000E+00
5/6	2/4	9.266E−03	9.076E−05
5/6	3/4	1.838E−04	3.386E−08
5/6	4/4	3.707E−08	2.878E−16

deformation being imposed for this cases. Obviously, for the other two cases, $\alpha = 0°$ and $\alpha = 90°$, the geometry, load and material symmetries lead to both symmetric deformed shapes. In these two cases, $\alpha = 0°$ and $\alpha = 90°$, (principal) stretches of about $\lambda_x \approx 2 \approx 1/\lambda_y$ ($E_{xx} \approx 0.7 \approx -E_{yy}$) are obtained in the central passing zone between the hole and the longest borders of the plate, hence the functions depicted in Fig. 3 are evaluated at almost their whole range of definition. As indicated above, for larger deformations, these spline-based functions should be accordingly extrapolated. Table 4 shows that quadratic force and energy rates of convergence are obtained in a typical step during the computations.

For comparison purposes, the same computations have been performed using the isochoric strain energy function $\mathcal{W}$ formed in this case by the three longitudinal terms ω_{ii}, $i = 1, 2, 3$, obtained in the previous Section for the case in which $\nu_{12} = 0.7$ (see their derivatives in Fig. 5) combined with, again, the three shear terms ω_{ij}, $i \neq j$, obtained in this Section (Fig. 6). The results obtained for $\alpha = 0°$, $\alpha = 30°$, $\alpha = 60°$ and $\alpha = 90°$ are shown in Fig. 9. From the comparison of Figures 8 and 9, we note that the stress values are larger in the first case due to the stiffer contribution of ω_{11} and ω_{22} (compare Figs. 3 and 5). Due to the plain strain condition being imposed, the contribution of ω_{33} is not relevant in any case. For this example, the combination of the horizontal displacement being prescribed, the plane strain condition and the incompressibility constraint generate little differences regarding deformations. Even though, from the computed results and the deformed configurations for the orientation $\alpha = 0^o$ depicted in Figures 8 and 9 (top configurations), we note that the dimension h of the deformed plate in the transverse direction y is larger in the first case, $h \approx 13.15 \, \text{mm}$ (for which $\nu_{12} = 0.3$ was prescribed to obtain $\mathcal{W}$) than in the second example, $h \approx 12.85 \, \text{mm}$ (with an strain energy function $\mathcal{W}$ determined for $\nu_{12} = 0.7$), as it should be. An analogous interpretation can be performed comparing the configurations for the orientation $\alpha = 90^o$ (bottom configurations in Figures 8 and 9) and taking into

account that the value $\nu_{21} = 0.260$ was obtained as a part of the solution during the determination of the strain energy function used in the first case and the value $\nu_{21} = 0.623$ was obtained for the strain energy function used in the second case.

Finally, we want to emphasize that the only reason for obtaining different stress and strain results in this example (under plain strain) is the selection of *a specific transverse strain distribution* $\tilde{E}_2^1(\tilde{E}_1^1)$ (or a equivalent Poisson's ratio ν_{12}) used as initial "experimental" data for the definition of the deviatoric strain energy function $\mathcal{W}$ given in Eq. (18). It is important to remark that the remaining five "experimental" curves are still very accurately replicated in both cases. Again, this fact indicates the importance of defining the *complete* set of experimental data indicated above (or other equivalent set), which should be accordingly captured by the selected stored energy function to be able to perform realistic Finite Element simulations.

5 Conclusions

In this paper we present a model for incompressible orthotropic hyperelasticity. The model is based on piecewise spline interpolations of the experimental data, from which the stored energy function if obtained. No specific shape is assumed for the stored energy function. On the contrary, the equilibrium equations of the corresponding set of six experimental tests are solved in order to obtain the function directly from those experimental stress-strain curves. We do not assume the existence of fibers and a matrix in the material, but consider the material as a whole. Hence, the model may be used for a wide range of hyperelastic materials, not only for fiber reinforced composites, and without the knowledge of the behavior of the isolated components. As a consequence of the procedure, the prescribed experimental data for all tests is "exactly" reproduced by the model.

The model is based on an energy form using a special decomposition of the stored energy function proposed in the spirit of the Valanis-Landel decomposition for isotropic materials which is exact for quadratic energy functions and which includes all structural invariants except one. Furthermore, the use of logarithmic strains in the formulation facilitates the interpretation of the model as a natural extension of the small strains one, a fact that is also in accordance to the experimental observations of Anand for some isotropic materials and with the geometric interpretation of the logarithmic strains.

Finally, we have shown that the procedure may facilitate excellent predictions for up to the six needed
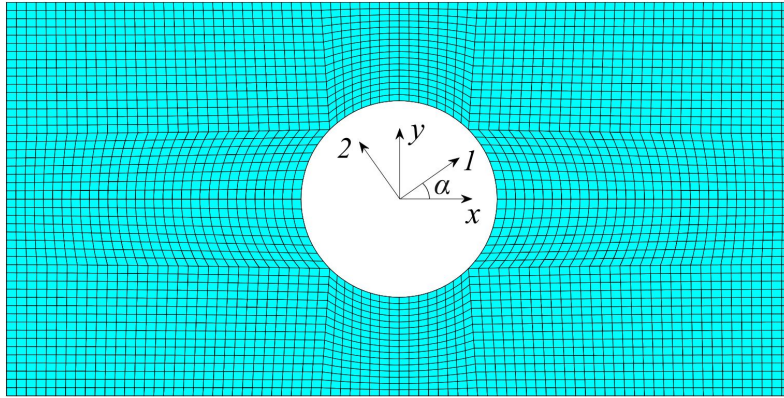
Fig. 7 Rectangular plate with a concentric hole: reference configuration, initial orientation (angle α) of the preferred material directions and finite element mesh. Dimensions of the plate: $l_0 \times h_0 \times t_0 = 32\,\text{mm} \times 16\,\text{mm} \times 0.5\,\text{mm}$. Radius of the hole: $r_0 = 4\,\text{mm}$

experiments to properly define the model. We also facilitate the constitutive tangent moduli for a finite element implementation and show that the formulation may be efficiently programmed in a finite element code in order to obtain predictions for more complex, non-proportional situations.

References

1. Bathe KJ (1996) Finite Element Procedures. Prentice-Hall, New Jersey.
2. Kojic M, Bathe KJ (2005) Inelastic Analysis of Solids and Structures. Springer-Verlag, New York.
3. Ogden RW (1997) Non-Linear Elastic deformations. Dover Publications, Mineola, New York.
4. Montáns FJ, Bathe KJ (2007) Towards a model for large strain anisotropic elasto-plasticity. In: Onate E, Owen R (ed) Computational Plasticity. Springer-Verlag, Netherlands, pp 13–36.
5. Caminero MÁ, Montáns FJ, Bathe KJ (2011) Modeling large strain anisotropic elasto-plasticity with logarithmic strain and stress measures. Comp Struct 89:826–843.
6. Kojic M, Bathe KJ (1987) Studies of Finite Element Procedures Stress Solution of a Closed Elastic Strain Path with Stretching and Shearing using the Updated Lagrangian Jaumann Formulation. Comp Struct 26(1/2):175–179.
7. Ogden RW (1972) Large deformation isotropic elasticity: on the correlation of theory and experiment for incompressible rubberlike solids. Proc R Soc Lond A 326:565–584.
8. Mooney M (1940) A theory of large elastic deformation. J App Phys 11:582–592.
9. Rivlin RS (1948) Large Elastic Deformations of Isotropic Materials. IV. Further Developments of the General Theory. Phil Trans R Soc Lond A 241(835):379–397.
10. Blatz PJ, Ko WL (1962) Application of finite elasticity theory to the deformation of rubbery materials. Trans Soc Rheol 6:223–251.
11. Yeoh OH (1990) Characterization of elastic properties of carbon-black-filled rubber vulcanizates. Rubber Chem Tech 63:792–805.
12. Arruda EM, Boyce MC (1993) A three-dimensional constitutive model for the large stretch behavior of rubber elastic materials. J Mech Phys Sol 41:389–412.
13. Twizell EH, Ogden RW (1983) Non-linear optimization of the material constants in Ogden's stress-deformation function for incompressible isotropic elastic materials. J Austral Math Soc B 24:424–434.
14. Itskov M (2001) A generalized orthotropic hyperelastic material model with application to incompressible shells. Int J Num Meth Eng 50:1777–1799.
15. Itskov M, Aksel N (2004) A class of orthotropic and transversely isotropic hyperelastic constitutive models based on a polyconvex strain energy function. Int J Sol Struct 41:3833–3848.
16. Gasser TC, Ogden RW, Holzapfel GA (2006) Hyperelastic modelling of arterial layers with distributed collagen fibre orientations. J R Soc Interface 3:15–35.
17. Holzapfel GA, Ogden RW (2009) Constitutive modelling of passive myocardium: a characterization structurally based framework for material characterization. Phil Trans R Soc A 367:3445–3475.
18. Holzapfel GA, Gasser TC (2000) A New Constitutive Framework for Arterial Wall Mechanics and a Comparative Study of Material Models. J Elast 61:1–48.
19. Sussman T, Bathe KJ (2009) A Model of Incompressible Isotropic Hyperelastic Material Behavior using Spline Interpolations of Tension-Compression Test Data. Commun Num Meth Eng 25:53–63.
20. Kearsley EA and Zapas LJ (1980) Some Methods of Measurement of an Elastic Strain-Energy Function of the Valanis-Landel Type. J Rheol 24:483–501.
21. Latorre M, Montáns FJ (2013) Extension of the Sussman–Bathe spline-based hyperelastic model to incompressible transversely isotropic materials. Comp Struct 122:13–26.
22. Latorre M, Montáns FJ (submitted) On the interpretation of the logarithmic strain tensor in an arbitrary system of representation.
23. Valanis KC, Landel RF (1967) The Strain-Energy Function of a Hyperelastic Material in Terms of the Extension Ratios. J App Phys 38:2997–3002.
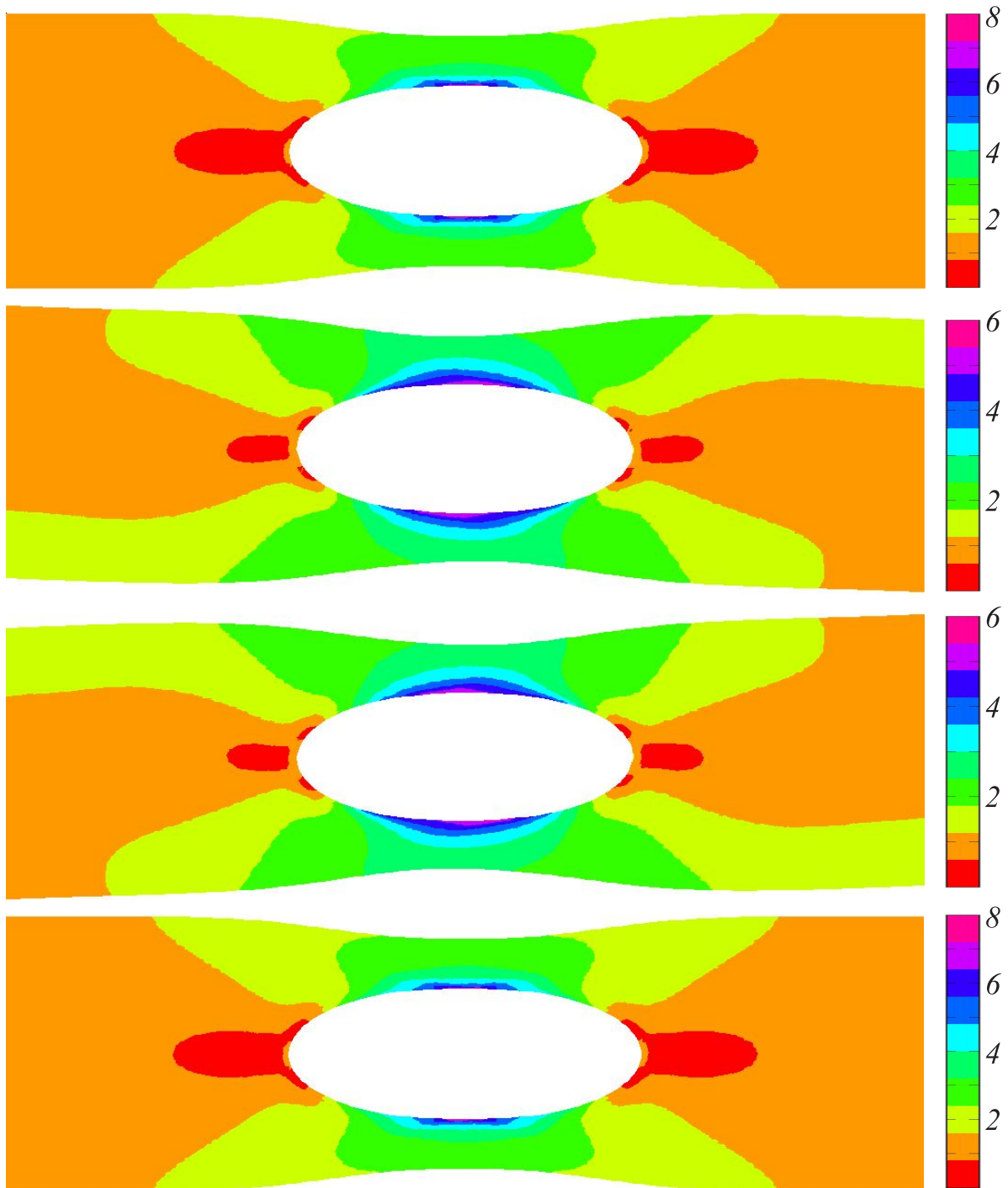24. Montáns FJ, Benítez JM, Caminero MÁ (2012) A large strain anisotropic elastoplastic continuum theory for non-

Fig. 8 Uniaxial tension of a rectangular plate with a concentric circular hole under a plain strain condition: Deformed configuration ($length = 44$ mm) and distribution of the deviatoric Cauchy stress norm $\left\|\boldsymbol{\sigma}^{iso}\right\| = \sqrt{\boldsymbol{\sigma}^{iso} : \boldsymbol{\sigma}^{iso}}$ (MPa) for $\alpha = 0°$, $\alpha = 30°$, $\alpha = 60°$ and $\alpha = 90°$ (from top to bottom) using the isochoric strain energy function $\mathcal{W}$ of Eq. (18) with the spline-based terms from Figures 3 and 6. Unaveraged results at nodes. Upper limit of each color scale is defined by the maximum value (approx.) taken by $\left\|\boldsymbol{\sigma}^{iso}\right\|$ for each case
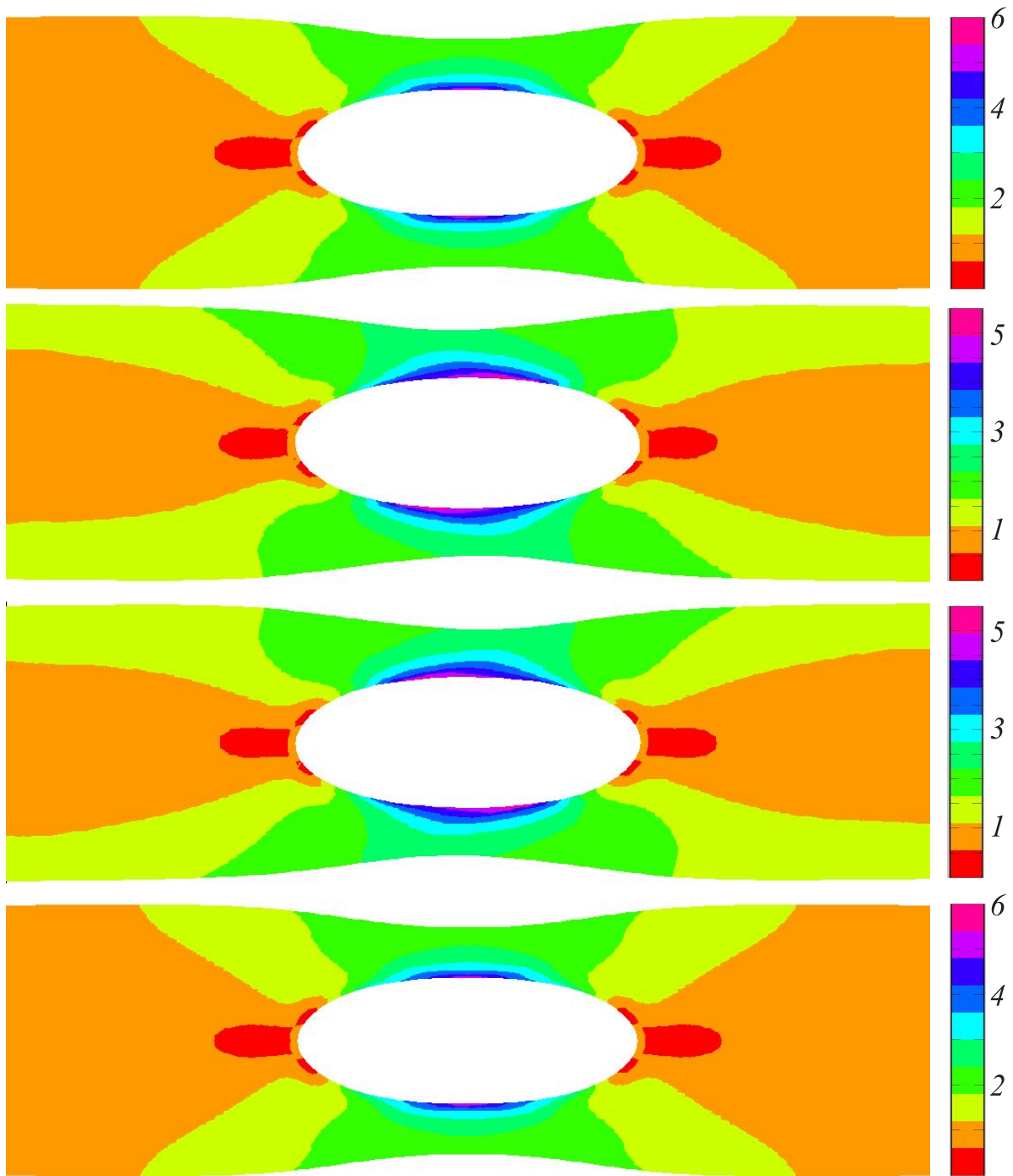
Fig. 9 Uniaxial tension of a rectangular plate with a concentric circular hole under a plain strain condition: Deformed configuration ($length = 44\,\mathrm{mm}$) and distribution of the deviatoric Cauchy stress norm $\left\|\boldsymbol{\sigma}^{iso}\right\| = \sqrt{\boldsymbol{\sigma}^{iso} : \boldsymbol{\sigma}^{iso}}$ (MPa) for $\alpha = 0°$, $\alpha = 30°$, $\alpha = 60°$ and $\alpha = 90°$ (from top to bottom) using the isochoric strain energy function $\mathcal{W}$ of Eq. (18) with the spline-based terms from Figures 5 and 6. Unaveraged results at nodes. Upper limit of each color scale is defined by the maximum value (approx.) taken by $\left\|\boldsymbol{\sigma}^{iso}\right\|$ for each case

linear kinematic hardening and texture evolution. Mech Res Commun 43:50–56.

25. Miehe C, Lambrecht M (2001) Algorithms for computation of stresses and elasticity moduli in terms of Seth–Hill's family of generalized strain tensors. Commun Num Meth Eng 17:337–353.

26. Anand L (1979) On H. Hencky's approximate strain-energy function for moderate deformations. J App Mech 46:78–82.

27. Anand L (1986) Moderate deformations in extension-torsion of incompressible isotropic elastic materials. J Mech Phys Sol 34:293–304.

28. Morrow DA, Donahue TLH, Odegard GM, Kaufman KR (2010) Transversely isotropic tensile material properties of skeletal muscle tissue. J Mech Behav Biomed Mater 3:124–129.

29. Holzapfel GA, Sommer G, Gasser TC, Regitnig P (2005) Determination of layer-specific mechanical properties of human coronary arteries with nonatherosclerotic intimal thickening and related constitutive modeling. Am J Physiol Heart Circ Physiol 289:2048–2058.

30. Sacks MS (1999) A method for planar biaxial mechanical testing that includes in-plane shear. J Biomech Eng 121(5):551–555.

31. Dokos S, Smaill BH, Young AA, LeGrice IL (2002) Shear properties of passive ventricular myocardium. Am J Physiol Heart Circ Physiol 283:2650–2659.

32. Diani J, Brieu M, Vacherand JM, Rezgui A (2004) Directional model for isotropic and anisotropic hyperelastic rubber-like materials. Mech Mater 36:313–321.

33. Sussman T, Bathe KJ (1987) A finite element formulation for nonlinear incompressible elastic and inelastic analysis. Comp Struct 26:357–409.

34. Hartmann S, Neff P (2003) Polyconvexity of generalized polynomial-type hyperelastic strain energy functions for near-incompressibility. Int J Sol Struct 40:2767–2791.